

Distance estimation of gamma-ray emitting BL Lac objects from imaging observations

K. Nilsson^{1,*}, V. Fallah Ramazani^{1,2}, E. Lindfors^{1,3}, P. Goldoni⁴, J. Becerra González^{5,6}, J. A. Acosta Pulido^{5,6}, R. Clavero^{5,6}, J. Otero-Santos^{5,6,7}, T. Pursimo⁸, S. Pita⁴, P. M. Kouch^{1,3}, C. Boisson⁹, M. Backes^{10,11}, G. Cotter¹², F. D'Ammando¹³, and E. Kasai¹⁰

¹ Finnish Centre for Astronomy with ESO (FINCA), Quantum, Vesilinnantie 5, FI-20014 University of Turku, Finland

² Aalto University Metsähovi Radio Observatory, Metsähovintie 114, 02540, Kylmälä, Finland

³ Department of Physics and Astronomy, University of Turku, Finland

⁴ Université Paris Cité, CNRS, CEA, Astroparticule et Cosmologie, F-75013 Paris, France

⁵ Universidad de La Laguna (ULL), Departamento de Astrofísica, E-38206 La Laguna, Tenerife, Spain

⁶ Instituto de Astrofísica de Canarias (IAC), E-38200 La Laguna, Santa Cruz de Tenerife, Spain

⁷ Instituto de Astrofísica de Andalucía (CSIC), Glorieta de la Astronomía s/n, 18008 Granada, Spain

⁸ Nordic Optical Telescope, Apartado 474, E-38700 Santa Cruz de La Palma, Spain

⁹ Laboratoire Univers et Théories, Observatoire de Paris, Université PSL, Université Paris Cité, CNRS, F-92190 Meudon, France

¹⁰ Department of Physics, Chemistry & Material Science, University of Namibia, Private Bag 13301, Windhoek, Namibia

¹¹ Centre for Space Research, North-West University, Potchefstroom 2520, South Africa

¹² Oxford Astrophysics, University of Oxford, Denys Wilkinson Building, Keble Road, Oxford, OX1 3RH, United Kingdom

¹³ INAF - Istituto di Radioastronomia, Via Gobetti 101, I-40129 Bologna, Italy

Received September 15, 2023; accepted September 16, 2023

ABSTRACT

Aims. Direct redshift determination of BL Lac objects is highly challenging as the emission in the optical and near-infrared (NIR) bands is largely dominated by the non-thermal emission from the relativistic jet that points very close to our line of sight. Therefore, their optical spectra often show no emission lines from the host galaxy. In this work, we aim to overcome this difficulty by attempting to detect the host galaxy and derive redshift constraints based on assumptions on the galaxy magnitude ("imaging redshifts").

Methods. Imaging redshifts are derived by obtaining deep optical images under good seeing conditions, so that it is possible to detect the host galaxy as weak extension of the point-like source. We then derive the imaging redshift by using the host galaxy as a standard candle using two different methods.

Results. We determine imaging redshift for 9 out of 17 blazars that we observed as part of this program. The redshift range of these targets is 0.28-0.60 and the two methods used to derive the redshift give very consistent results within the uncertainties. We also performed a detailed comparison of the imaging redshifts with those obtained by other methods, like direct spectroscopic constraints or looking for groups of galaxies close to the blazar. We show that the constraints from different methods are consistent and that for example in the case of J2156.0+1818, which is the most distant source for which we detect the host galaxy, combining the three constraints narrows down the redshift to $0.63 < z < 0.71$. This makes the source interesting for future studies of extragalactic background light in the Cherenkov Telescope Array Observatory era.

Key words. Galaxies:active – Galaxies:distances and redshifts – Gamma rays:galaxies

1. Introduction

Blazars are active galactic nuclei (AGN) in which relativistic jets, launched by supermassive black holes, point very close to our line of sight. They are the most numerous extragalactic gamma-ray ($E = 100 \text{ keV} - 100 \text{ GeV}$, Ajello et al. 2020) and very-high-energy (VHE, $E = 100 \text{ GeV} - 100 \text{ TeV}$, Wakely & Horan 2008) gamma-ray sources and candidate sources of very high energy astrophysical neutrinos detected by the IceCube Neutrino Observatory (IceCube Collaboration et al. 2018).

Blazars are classified into flat spectrum radio quasars (FSRQs) and BL Lacertae (BL Lac) objects. The distinctive feature between the two classes is the presence of broad (few thousand km/s) and luminous ($\geq 10^{42} \text{ erg s}^{-1}$) emission lines in the optical spectra of the former and their weakness or absence in

the latter. The limit is usually set at an equivalent width EW of 5 \AA (Urry & Padovani 1995) but it is known that EW emission lines of BL Lacs can sometimes get larger than that (see e.g. Stickel et al. 1991). One challenge in studies of the many key questions of blazar physics is the difficulty of obtaining redshifts from their nearly featureless, continuum-dominated spectra. High signal-to-noise spectra are needed to detect those weak lines and, therefore, a large fraction of BL Lacs ($\sim 59\%$) have no firmly established redshifts still today (Massaro et al. 2015a).

For BL Lac objects, it is in many cases easier to detect the host galaxy via deep optical and NIR imaging than the weak emission and absorption lines. It was shown by Sbarufatti et al. (2005a) that the distribution of BL Lac host galaxy absolute magnitudes M_R is almost Gaussian with an average value of -22.9 and $\sigma = 0.5$. Therefore, BL Lac host galaxies can be used as "standard candles" to estimate their distances. This result was

* e-mail: kani@utu.fi

later confirmed by [Shaw et al. \(2013\)](#), albeit with slightly different mean absolute magnitude. Due to the width of the host galaxy luminosity distribution this redshift estimate has a $1\text{-}\sigma$ error of at least 0.05 at $z=0.3$ or about 16%, while spectroscopic redshift errors are regularly smaller than 0.1%.

Even if this method is less accurate than spectroscopic determination, it still gives an estimate of the distance of the source. In addition, it has been shown that for the sources where the host galaxy is detected in imaging, the spectroscopic observations are more likely to detect lines for more accurate redshift determination ([Nilsson et al. 2003](#); [Goldoni et al. 2021](#); [D’Ammando et al. 2024](#)). Furthermore, the accurate determination of the host galaxy magnitude from imaging observations also allows us to estimate the mass of the supermassive black hole (M_{BH}), a parameter that has been suggested to significantly correlate with the shape of the emitted spectral energy distribution (SED) and its bolometric luminosity ([Ghisellini et al. 2011](#)).

In the next few years a new facility, the Cherenkov Telescope Array Observatory (CTAO), will become operational with a northern site in the Canary Islands (Spain) and a southern site in the Atacama desert (Chile). It will have a 20 GeV - 300 TeV energy range and a sensitivity approximately 10 times better than the current facilities in this energy range. Blazars are the main extragalactic targets for CTAO, which is expected to detect hundreds of blazars according to current estimates, thus opening the possibility of population studies with a significant sample size ([Cherenkov Telescope Array Consortium et al. 2019](#)). The planning of observations by the CTAO Consortium is currently ongoing. It is therefore of great importance to start acquiring redshifts and properties of the host galaxies for a large fraction of the AGN sources detected with *Fermi*-LAT that are likely to be detected with CTAO. There is, therefore, a redshift measuring campaign from which three papers have recently been published. [Goldoni et al. \(2021\)](#) contains spectroscopic measurements of 19 BL Lac objects, resulting in determination of 11 new high-confidence redshifts, one tentative redshift and three lower limits to redshift. In [Kasai et al. \(2023\)](#), 25 high-quality spectra are presented, resulting in 14 confirmed redshifts. In [D’Ammando et al. \(2024\)](#), 24 high quality spectra resulted in 12 confirmed redshifts, one tentative redshift and two lower limits.

In this paper, we present I-band imaging of a sample of 17 blazars. The sample selection is summarised in Section 2 and the deep optical imaging observations in Section 3. The analyses to derive the imaging redshifts are explained in Section 4 and the results of these analyses in Section 5. The discussion of how the derived constraints on redshift of the sources compare with redshifts derived by other methods is presented in Section 6 and summary and conclusions are presented in Section 7. Throughout this paper we use the cosmology $H_0 = 70 \text{ km s}^{-1} \text{ Mpc}^{-1}$, $\Omega_\Lambda = 0.7$ and $\Omega_M = 0.3$.

2. Sample selection

This paper is part of a larger redshift determination program and therefore the initial step of the sample selection was performed as in [Goldoni et al. \(2021\)](#), [Kasai et al. \(2023\)](#) and [D’Ammando et al. \(2024\)](#). *Fermi*-LAT has detected more than 3130 active galactic nuclei (4FGL catalogue; [Abdollahi et al. 2020](#)). The sources that are detected above 10 GeV by *Fermi*-LAT (3FHL [Ajello et al. 2017](#)) have good potential to be detected also with CTAO. 3FHL contains 1040 BL Lacs and Blazar candidates of an unknown type (BCUs) and initially for 64% of the sources the redshifts are unknown. The 3FHL spectra, that typically represent the average flux state of the source, are extrapolated to

the VHE γ -ray band, but adding cut-off at 3 TeV. Absorption by the extragalactic background light (EBL) has also to be accounted for, but to account for it correctly, we would obviously need the redshift of the sources. At the time of the selection, we did not have spectroscopic redshifts for the sources and therefore used $z=0.3$ for all sources. The EBL model from [Domínguez et al. \(2011\)](#) was used to calculate the gamma-ray absorption. The Monte Carlo simulations of the detectability with CTAO were performed with the Gammapy software¹ and the publicly-accessible CTAO performance files. The sources that are detectable at 5σ in 30 hours of observations with CTAO and have unknown redshift were selected for this redshift program. The full sample consists of 165 sources.

In this paper we present deep I-band imaging observations of a sub-sample of 17 sources for which we could not find evidence of extension or deep imaging observations from the literature. This program started in 2016, so for some sources spectroscopic redshifts have been obtained, some of them as follow-up of these imaging observations. In that case, we re-evaluated the detectability with CTAO using the actual redshift. The observation times for CTAO to detect these sources are given in Table 1.

3. Observations

The observations were carried out with the Nordic Optical Telescope (NOT)². The objects of our sample were observed by NOT between 2016 and 2019 using the Alhambra Faint Object Spectrograph and Camera³ (ALFOSC) in *I*-band⁴. This instrument has a field of view of 6.4×6.4 arcmin with pixel scale of 0.21 arcsec/pix., gain 0.15 e^-/ADU and readout noise 4.3 e^- . The dark current is negligible due to liquid nitrogen cooling (0.03 $e^-/\text{pix/h}$ at $T_{\text{operation}} = -120^\circ \text{C}$). The observations were performed in I-band during good seeing conditions to maximise the probability of detecting the host galaxy. The details of the observations are given in Table 2.

4. Analysis

The main goal of the analysis is to obtain the host galaxy luminosities and effective radii, which can then be used to derive the redshift using two methods described in more detail below. For this purpose we fitted two-dimensional models to the observed light distribution.

Prior to the fitting, the images were reduced in the standard way of bias subtraction and flat-fielding, after which the individual images were registered using suitable stars in the field and summed. Calibration of the summed images was achieved through the stars with known magnitudes in the blazar fields. We first matched the positions of isolated stars in the field with positions in the PAN-STARRS survey catalogue ([Chambers et al. 2016](#)). The number of matched stars varied from 7 to 77 per field. We then obtained their *i* and *z*-band aperture magnitudes from PAN-STARRS and transformed them to Cousins I-band via the formula⁵

¹ <https://gammapy.org/>

² The Nordic Optical Telescope is located at Observatorio del Roque de los Muchachos, La Palma, Canary Islands, Spain. Its primary mirror diameter is 2.56 m.

³ <http://www.not.iac.es/instruments/alfosc/>

⁴ <http://www.not.iac.es/instruments/filters/curves/png/12.png>

⁵ <https://live-sdss4org-dr12.pantheonsite.io/algorithms/sdssUBVRITransform/#Lupton200>

Table 1. General properties of the sample.

(1)	(2)	(3)	(4)	(5)	(6)	(7)
Source name	3FHL Name	RA J2000	Dec J2000	z	ref	CTA Exp. (hours)
GB6 J0045+2127	J0045.3+2127	00 45 19.30	21 27 40.10	0.4253	1	2.5
GB6 J0148+5202	J0148.2+5201	01 48 20.25	52 02 05.80	0.437	1	42.0
GB6 J0905+1358	J0905.5+1357	09 05 34.99	13 58 06.30	0.2239,0.644*	1	8.1,20.5
Ton 396	J0915.9+2933	09 15 52.40	29 33 24.04			15.5
RBS 1040	J1150.5+4154	11 50 34.76	41 54 40.09			14.8
1RXS J154604.6+081912	J1546.1+0818	15 46 04.30	08 19 14.00	>0.513	2	63.6
PG 1553+113	J1555.7+1111	15 55 43.04	11 11 24.36	0.43	3	0.1
1RXS J181118.3+034109	J1811.3+0341	18 11 18.09	03 41 13.90			11.8
NVSS J184425+154646	J1844.4+1546	18 44 25.34	15 46 46.00			47.7
1RXS J193109.5+093714	J1931.1+0937	19 31 09.23	09 37 16.40	>0.476	4	1.8
1RXS J193320.3+072616	J1933.3+0726	19 33 20.30	07 26 16.00			5.7
1RXS J194246.3+103339	J1942.7+1033	19 42 47.48	10 33 27.80			0.9
RX J2030.8+1935	J2031.0+1936	20 30 57.13	19 36 12.91	0.3665	5	35.0
RX J2156.0+1818	J2156.0+1818	21 56 01.63	18 18 39.20	>0.6347	6	31.3
NVSS J224604+154437	J2245.9+1545	22 46 04.99	15 44 37.50	0.5966	5	65.1
1RXS J224753.3+441321	J2247.9+4413	22 47 53.21	44 13 15.30			23.9
1RXS J230437.1+370506	J2304.7+3705	23 04 36.80	37 05 07.00			27.5

Notes. Columns: (1) source name, (2) source name in 3FHL catalogue, (3) right ascension, (4) declination, (5) assumed redshift, (6) redshift reference, (7) CTA exposure time for the detection of the source at VHE gamma rays using the redshift or lower limit in the table or $z = 0.3$ if no redshift is available.

* See section 6.1 for details about the redshift values.

Redshift references: (1) [Paiano et al. \(2020\)](#), (2) [Ahumada et al. \(2020\)](#) (3) [Johnson et al. \(2019\)](#) (4) [Shaw et al. \(2013\)](#) (5) [Kasai et al. \(2023\)](#) (6) [D'Ammando et al. \(2024\)](#).

Table 2. Logbook of the observations.

(1)	(2)	(3)	(4)	(5)	(6)	(7)
3FHL name	Date	N	Exp. (s)	FWHM (arcsec)	Airmass range	Ap mag
J0045.3+2127	2019-08-30	20	2900	0.59	1.01-1.07	16.57
J0148.2+5201	2019-08-30	10	1900	0.69	1.09-1.11	16.92
J0905.5+1357	2019-03-02, 2019-03-01	27	4680	0.70	1.03-1.07	16.35
J0915.9+2933	2018-01-10	81	2430	0.74	1.05-1.20	15.40
J1150.5+4154	2019-03-01, 2019-05-06	43	5130	0.76	1.04-1.06	16.04
J1546.1+0818	2019-05-07, 2019-06-17	36	3600	0.69	1.06-1.08	16.64
J1555.7+1111	2019-05-06, 2019-06-17	63	315	0.67	1.06-1.15	12.94
J1811.3+0341	2019-08-29	7	2900	0.90	1.10-1.13	16.25
J1844.4+1546	2019-08-29	10	2250	0.86	1.08-1.16	16.46
J1931.1+0937	2016-10-01	10	2000	0.78	1.20-1.34	16.14
J1933.3+0726	2017-06-19	12	2400	0.57	1.07-1.09	16.58
J1942.7+1033	2016-10-09	12	1400	0.51	1.32-1.51	15.61
J2031.0+1936	2019-05-07, 2019-06-20	16	3200	0.72	1.04-1.21	17.24
J2156.0+1818	2019-08-30	20	2850	0.70	1.02-1.05	16.79
J2245.9+1545	2019-08-30	6	3000	0.74	1.02-1.03	18.15
J2247.9+4413	2017-07-26	12	2400	0.59	1.29-1.48	16.93
J2304.7+3705	2017-08-11	12	2400	1.00	1.01-1.03	17.17

Notes. Columns: (1) source name in 3FHL catalogue, (2) date(s) of observation, (3) number of images combined, (4) total exposure time in seconds, (5) seeing (FWHM) in arcsec which is calculated by fitting a Gaussian profile to a star close to the target, (6) airmass range during the exposures and (7) I-band magnitude through a 5 arcsec diameter aperture. The error is 0.02 mag.

$$I = i - 0.3780(i - z) - 0.3974.$$

After performing aperture photometry to the stars in our images, we derived the zero point for each field as the average difference between our and the transformed PAN-STARRS magnitudes. The rms scatter of the magnitude differences was generally found to be very small, about 0.01-0.02 mag per field, even

for fields with the most numerous matches, thus showing that our calibration is accurate.

After calibration the local background near the blazar value was determined from 5-7 empty sky regions within ~ 10 arcsec of the target and subtracted. A final check was made to ensure that there are no subtle slopes in the background. In the few cases a slope was found, it was corrected by fitting a plane to the pure sky emission around the target and subtracting the fit. Then we

determined if there were any stars, galaxies, blemishes, etc. overlapping the blazar image and masked any affected pixels out of the fit. Finally, we visually determined the radius beyond which no blazar light (from host galaxy and nucleus) was visually detectable and restricted the fit inside this area.

Our model for the light distribution of blazars consists of two components, the unresolved AGN (hereafter the "core") and the host galaxy. Three parameters, (x_c, y_c) position plus magnitude m_c are sufficient to fully describe the core, whereas 7 parameters are needed for the host galaxy: position (x_g, y_g) , assumed to be the same as the core), magnitude m_g , effective radius r_{eff} , ellipticity ϵ , major axis position angle θ and the Sèrsic index n , which determines how centrally concentrated the light distribution is by assuming that the light follows the Sèrsic profile

$$I(R) = I_e \exp \left\{ -b_n \left[\left(\frac{R}{R_e} \right)^{1/n} - 1 \right] \right\}. \quad (1)$$

where R_e is the half-light radius, I_e is the intensity at R_e , and b_n is a coefficient which depends on the Sèrsic index n .

The models were convolved with a point-spread function (PSF) obtained from a high S/N star as close as possible to the target. We prefer an empirical PSF over an analytical one since, according to our experience, the former better represents the complexities of the PSF, especially for images like ours that are made by summing data taken over a course of several hours. Empirical PSFs contain observational noise, but this noise can be made insignificant by using a sufficiently bright star for the PSF. As discussed in e.g. Nilsson et al. (2003), the PSF shape depends on the position on the ALFOSC CCD. We did not attempt to model this, but rather included it in our noise model (see below).

For the fitting we used the downhill simplex method to find the set of parameters that minimises the chi square between the data and model. To compute the chi square we assumed the noise in each pixel to consist of three components, summed in quadrature to calculate the total noise per pixel: photon noise, readout noise and PSF error. The first two can be computed from the effective gain and the effective read out noise. The PSF error was assumed to be equal to a Gaussian function centred on the target with a width equal to the FWHM of the image and an amplitude of A times the peak value of the target. This noise component is significant only close to the centre of the target due to the quick tapering of the Gaussian function. A reasonable range for A is 0.01-0.1. We checked through simulations how the fit results depend on the choice of A . We found that, within the above range of A , the fit results are not biased in any significant way by the choice of A . However, the scatter of retrieved host galaxy parameters increases with increasing A . This happens because as A increases, the PSF noise becomes a more significant, and eventually dominant, noise source at the centre of the target. The central pixels contribute less and less to the total chi square sum, making the chi square space "flatter," thus increasing the scatter in the retrieved parameters. We found $A = 0.03$ to provide a reasonable estimate of the PSF errors for our data and adopted this value for all targets.

The fits were done in two stages: we first fitted a pure AGN model (x_c, y_c, m_c) to the image to fix the position and to look for any excess light in the residual image indicative of a host galaxy. In practice, if the core-subtracted image showed no residuals beyond PSF errors, we marked the target as unresolved, since experience has shown that no host galaxy is detected by the fit in this case (typically r_{eff} tends towards zero or infinity). In case any

residuals were detected, we moved to stage 2 by fixing the core and the host to the position obtained in stage 1. Since the host galaxies are typically very small and the unresolved core complicates the host characterisation, we did not attempt a detailed analysis of the host morphology. Therefore, we fixed ellipticity ϵ and position angle θ to 0 and let only the host magnitude m_g and effective radius r_{eff} to vary freely. Thus the second stage had 3 free parameters as well $(m_c, m_g, r_{\text{eff}})$. Stage 2 was done for two Sèrsic indices, $n = 1$ and $n = 4$ with the first representing a disk-dominated galaxy and the latter a bulge-dominated galaxy. We find that $n = 4$ consistently gives a better fit to these observations, and, except where noted, the results presented are for the $n = 4$ case.

We used two different methods to estimate the blazar redshift. Firstly, the results by Sbarufatti et al. (2005a) and Shaw et al. (2013) show that the BL Lac host galaxy luminosities are confined to a relatively narrow range of ± 0.5 mag. The former obtained average luminosity $M_R = -22.9$, whereas the latter $M_R = -22.5$. The latter also discuss two likely reasons for the difference in these results. Firstly, the Shaw et al. (2013) sample may contain fainter hosts simply for the reason that the more luminous hosts were already discovered by the time of their survey since they are easier to detect. The other reason may be a difference in the mixture of low energy peaked (LBL) and high energy peaked (HBL) BL Lacs between the samples. For our analysis we assume that $M_R = -22.7$ and that $R - I = 0.62$ at $z=0$. The latter value was determined by integrating an elliptical galaxy template spectrum of Mannucci et al. (2001) over the R-band and NOT I-band band-passes. Since the transformation from apparent to absolute magnitudes depends on redshift z , we have to find z iteratively. Because we also want to obtain an estimate of the uncertainty of z , we repeat the redshift iteration 1000 times each with different inputs. Thus we had two loops, the inner loop performing the z iteration and the outer loop repeating this iteration 1000 times.

For each z iteration we first drew the observed I-band magnitude of the host galaxy m_I from a Gaussian distribution with a mean and σ equal to the observed I-band magnitude and its error, respectively, and corrected it for Galactic absorption. Similarly, we drew a value for the host galaxy luminosity M_R from a Gaussian distribution with mean $= -22.7$ and $\sigma = 0.5$ and transformed that to M_I . Then we made a first guess of the redshift $z = z_0$ and computed the K-correction $K(z_0)$ and evolution correction $e(z_0)$ corresponding to this guess. The K-correction was computed from a fit to the correction in Fukugita et al. (1995). For the evolution correction we used $E(z) = 0.84 \times z$. This relation was derived by using the Pegase 3 code (Fioc & Rocca-Volmerange 2019) with a single starburst 10 Gyr ago and passive evolution thereafter. After this we derived the distance modulus

$$m - M = m_I - M_I - K(z_0) + E(z_0) \quad (2)$$

and the corresponding redshift z_1 from

$$m - M = 5 \log D_L + 5.0, \quad (3)$$

where D_L is the luminosity distance in parsecs. Since there is no closed form solution between z_1 and D_L , we interpolated the z_1 corresponding to D_L from a pre-computed table.

Then z_1 was used to calculate $K(z_1)$ and $E(z_1)$ to derive z_2 . This calculation was iteratively repeated until it stabilised, which typically happened after ~ 5 iterations and the resulting z was stored. After the outer loop was finished we computed the mean and standard deviation of the 1000 z estimates.

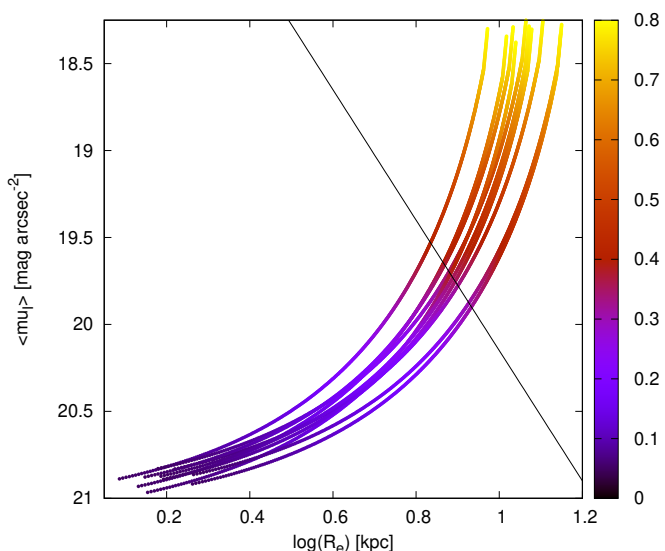


Fig. 1. Example of 10 runs with the "Kormendy" method for J0045.3+2127. Each run starts at $z=0.05$ in the lower left corner, moves up and right as z is increased and ends at $z=0.8$ as indicated by color. The line indicates the Kormendy relation of Eq. 4.

In the second method we assume that our host galaxies follow the Kormendy relation, i.e. the projection of the fundamental plane to the $R_{\text{eff}} - \langle \mu \rangle$ axes of elliptical galaxies, where R_{eff} is the effective radius in kpc and $\langle \mu \rangle$ is the average surface brightness inside the effective radius. This method uses both the host galaxy brightness and the effective radius as input unlike the first method that uses only the brightness.

We used the i-band Kormendy relation derived in Samir et al. (2020) for the brightest cluster galaxies (BCGs)

$$\langle \mu \rangle = (3.75 \pm 0.04) * \log(R_{\text{eff}}/1 \text{ kpc}) + (16.40 \pm 0.04). \quad (4)$$

Although blazar host galaxies are typically not found in dense clusters (e.g. Wurtz et al. 1997), their luminosities are very similar to the BCGs. The redshift is found as follows: we start with a relatively low redshift $z = 0.05$ and compute the corresponding effective radius R_{eff} in kpc from the observed effective radius r_{eff} . Next, we compute $\langle \mu \rangle$ from the observed host galaxy magnitude m using and r_{eff}

$$\langle \mu \rangle = m + 2.5 \log(2\pi(r_{\text{eff}}/1 \text{ arcsec})^2) - K(z) + E(z) - 10 \log(1+z). \quad (5)$$

This will result in a point in the $R_{\text{eff}} - \langle \mu \rangle$ plane that lies below and left of the line defined by Eq. 4. Increasing the test redshift will cause the point to move up and towards the right, until at certain $z = z_{\text{best}}$ it eventually cuts through the line defined by Eq. 4 (see Fig. 1). The redshift at which this happens is then adopted as the redshift of the blazar. We repeated this process 1000 times drawing each time the host magnitude, host effective radius, Galactic absorption and the slope and intercept of Eq. 4 from their respective distributions and adopted the standard deviation of the z_{best} as the error for the z .

5. Results

The host galaxies of 9 out of 17 objects have been detected and the results of the AGN + host galaxy decomposition for these

sources are shown in Figure 2. The measured magnitudes and effective radii of the galaxies along with the resulting imaging redshifts using the two methods described in previous section are presented in Table 3. In all cases the imaging redshifts derived with the two methods agree very well within the uncertainties.

We also estimated lower limits of z for the unresolved targets by adding an elliptical galaxy with $M_R = -21.7$, i.e. 1 mag fainter than the average value, and $r_{\text{eff}} = 8$ kpc to the observed image at increasing redshifts. We then determined the redshift at which the host galaxy became visually undetectable. Since it is not easy to objectively determine what "not visible" means, we applied fairly conservative judgement and the resulting lower limits can also be considered very conservative.

The observations presented here had a good success rate of ($\sim 53\%$), similar to the previous work by (Nilsson et al. 2003), where 100 BL Lacertae objects were imaged through the R-band. It is well known that it is easier to detect the host galaxy when the core is in a low state. We have indeed tried to optimize the timing of our imaging and spectroscopic (see Goldoni et al. 2021) observations to lower states of the blazars, when we have this information available. To understand if the successful detections were preferentially the result of observations in a low state and to see if there is room for improvement for the ones we did not detect, we investigated the Zwicky Transient Facility (ZTF) light curves of the 12 of our sources that were observed with NOT in the ZTF era (i.e. after beginning of 2018). In Appendix A, we show these light curves. As can be seen, most of the 12 sources were observed in rather moderate activity state, i.e. we managed to avoid the brightest flares, but did not catch the minima of the light curves either. The three exceptions to this were 3FHL J1555.7+1111 (PG 1553+113), which we observed in rather high state (and did not detect the host), 3FHL J0905.5+1357 and 3FHL J2031.0+1936, which we did observe in low state (and detected the host galaxy). Judging from the light curves, all four sources (3FHL J0915.9+2933, 3FHL J1546.1+0818, 3FHL J1555.7+1111, 3FHL J1844.4+1546), for which we have the ZTF data and did not detect the host should be re-observed during lower brightness state (see also Section 6).

Three unresolved targets deserve further comment. Firstly, we did not mark 3FHL J1811.3+0341 (1RXS J181118.3+034109) as resolved, although our analysis gives $I_{\text{host}} = 19.22 \pm 0.20$ and $r_{\text{eff}} = 1.7 \pm 0.9$ arcsec. As can be seen from Fig. 3, the surface brightness profile is just above the PSF and the host is very weak compared to the core. Furthermore, there are numerous objects overlapping with the blazar, making it very hard to find pixels unaffected by them. For these two reasons it is very difficult to reliably characterise the host galaxy and derive its redshift.

Secondly, some earlier studies of 3FHL J0915.9+2933 have concluded that this object is not extended (Abraham et al. 1991; Nilsson et al. 2003) while Meisner & Romani (2010) found it extended with $i_{\text{gal}} \sim 18.45$. We see weak excess around the centre after subtracting the PSF from the position of 3FHL J0915.9+2933 (Fig 4). Fitting a AGN core + host galaxy model yields $i = 17.66 \pm 0.08$ and $r_{\text{eff}} = 1.0 \pm 0.2$ arcsec. There is a faint extension SW of centre (Fig. 4, upper row), also visible in the residual image of Nilsson et al. (2003) and some excess emission E of the target. Due to these anomalies, we do not attempt to estimate the redshift of this source. The residuals after subtracting the core correspond to $i = 18.20$, consistent with Meisner & Romani (2010).

Thirdly, 3FHL J1933.3+0726 shows very atypical features for a blazar (Fig. 4, lower row). This target is clearly resolved,

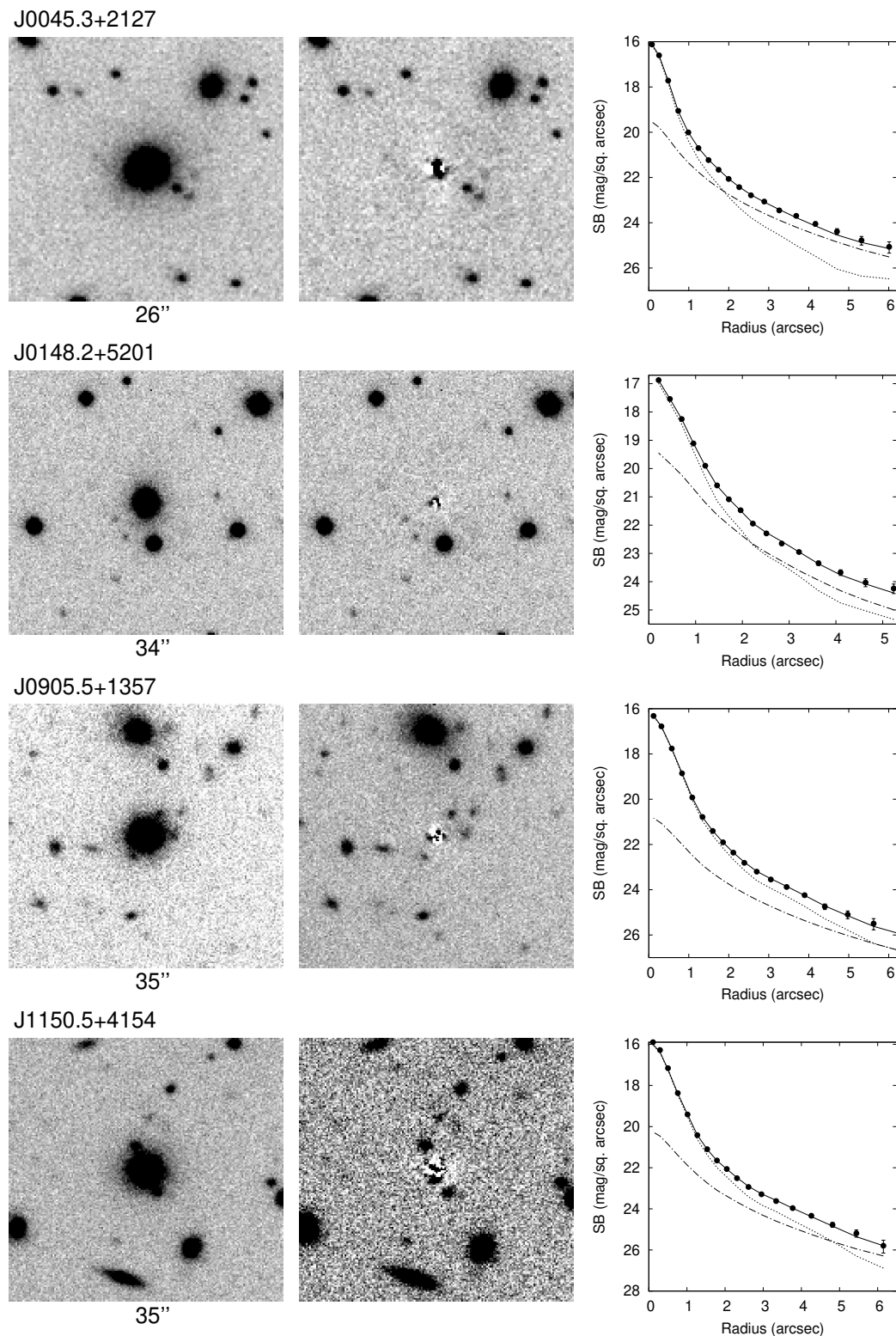


Fig. 2. Results of the AGN + host galaxy decomposition. *Left panel* : Greyscale image of the target. North is up and East is to the left. The field of view is given under the figure. *Middle panel*: the same image after subtracting the model. *Right panel*: Radial surface brightness profiles of the target (filled symbols), model (solid line), AGN nucleus (dashed line) and host galaxy (dot dashed line).

but the host galaxy type cannot be assigned since, unlike in all other targets, where the host galaxy fades smoothly into the background noise, the nebulosity around 3FHL J1933.3+0726 exhibits a relatively sharp edge, giving an impression of spiral galaxy seen face-on. The numerous targets overlapping the blazar and a CCD bleeding feature running over the core of

J1933.3+0726 further complicate the analysis. We used an iterative scheme in order to mitigate the effect of overlapping stars. We first performed PSF photometry on all bright targets near 3FHL J1933.3+0726 and subtracted them. Then we ran the model fit and subtracted the blazar model from the original image. The PSF photometry was repeated again on this subtracted

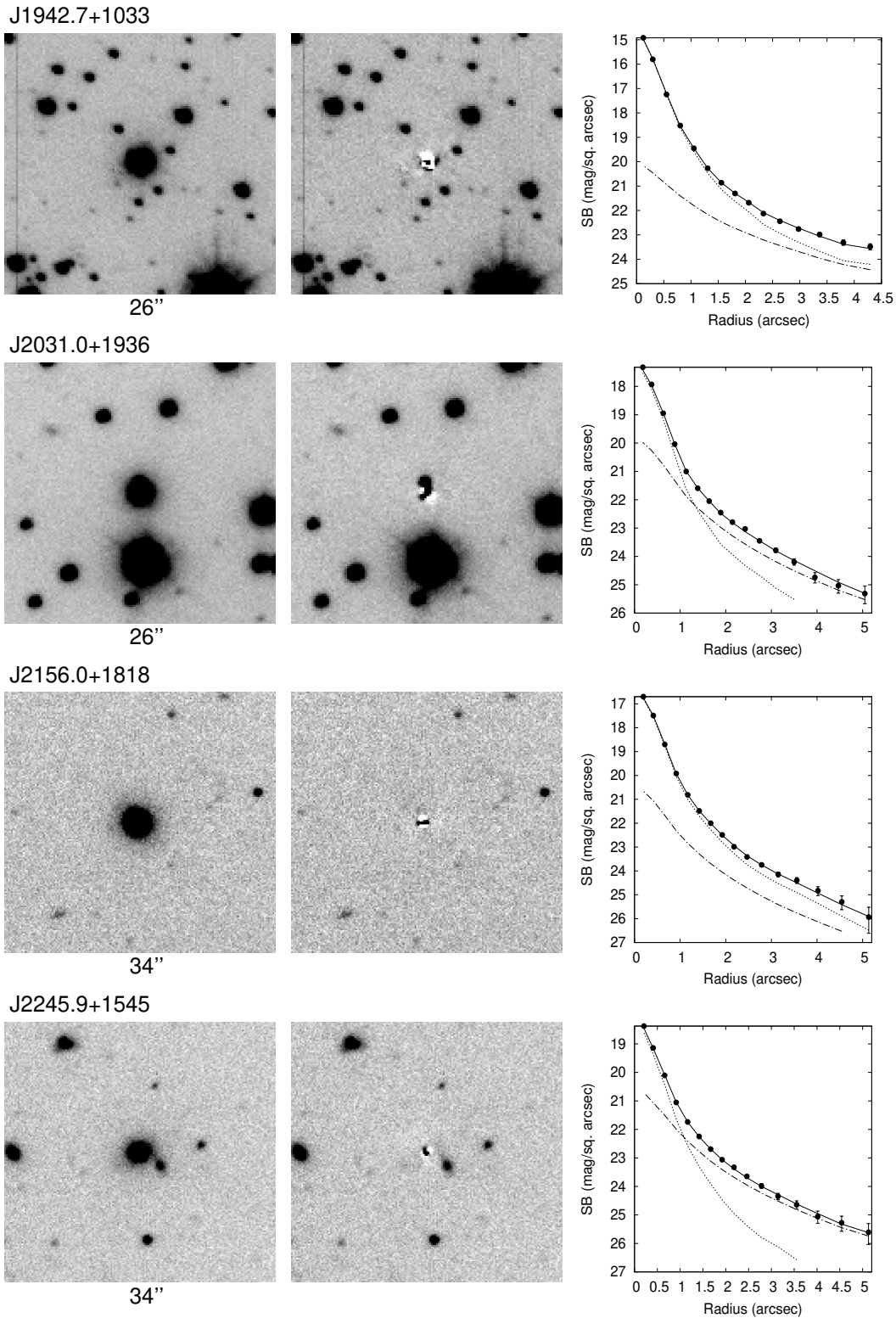


Fig. 2. –Continued

image after which model fitting was done again after subtracting the blazar model. After three iterations the fit results stabilized. This iteration was done using $n = 1$ and $n = 4$ and notably this is the only target where the $n = 1$ model gave a better fit to the data. However, significant residuals are still present in both cases. Given the peculiar morphology, the high number of over-

lapping targets and instrumental blemishes we did not attempt to derive a redshift for this target.

In one of the fields, 3FHL J1150.5+4154, the galaxies around the blazar seem to be distorted in a manner characteristic to gravitational lensing (Fig. 5). We made a simple study to see if we could establish this quantitatively by looking for an excess of galaxies with their sky projected major axes perpendic-

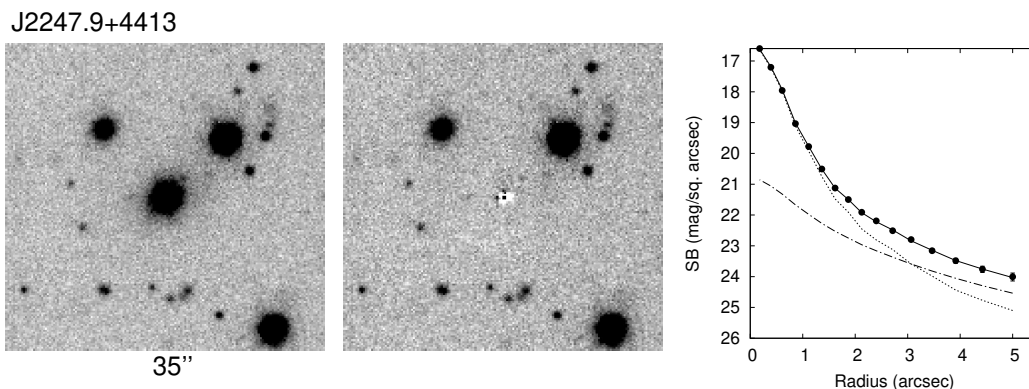


Fig. 2. –Continued

Table 3. Results of the host galaxy analysis.

(1)	(2)	(3)	(4)	(5)	(6)	(7)
3FHL name	I_{nucleus} (mag)	I_{galaxy} (mag)	r_{eff} (arcsec)	A_1 (mag)	z_1	z_2
J0045.3+2127	16.72 ± 0.02	17.99 ± 0.05	1.7 ± 0.2	0.018	0.34 ± 0.07	0.34 ± 0.04
J0148.2+5201	17.14 ± 0.03	18.31 ± 0.04	0.8 ± 0.2	0.025	0.38 ± 0.07	0.34 ± 0.07
J0905.5+1357	16.36 ± 0.02	19.03 ± 0.07	1.6 ± 0.5	0.053	0.50 ± 0.09	0.53 ± 0.12
J0915.9+2933	15.37 ± 0.02	17.66 ± 0.08	1.0 ± 0.2	0.037	†	
J1150.5+4154	16.05 ± 0.02	18.78 ± 0.11	2.9 ± 0.7	0.027	0.46 ± 0.09	0.54 ± 0.10
J1546.1+0818	16.54 ± 0.03	> 20.0		0.076	> 0.5	
J1555.7+1111	13.16 ± 0.03	> 17.7		0.078	> 0.2	
J1811.3+0341	16.15 ± 0.02	> 18.9		0.289	> 0.3	
J1844.4+1546	16.35 ± 0.01	> 19.3		0.687	> 0.3	
J1931.1+0937	16.14 ± 0.02	> 18.6		1.024	> 0.2	
J1933.3+0726	16.72 ± 0.03	†		0.452	†	
J1942.7+1033	15.61 ± 0.02	18.01 ± 0.12	3.1 ± 0.6	0.578	0.28 ± 0.06	0.31 ± 0.06
J2031.0+1936	17.47 ± 0.02	18.45 ± 0.07	1.8 ± 0.3	0.144	0.39 ± 0.08	0.40 ± 0.06
J2156.0+1818	16.79 ± 0.02	19.63 ± 0.12	1.4 ± 0.7	0.131	0.60 ± 0.11	0.62 ± 0.14
J2245.9+1545	18.45 ± 0.02	18.74 ± 0.11	2.4 ± 0.5	0.116	0.44 ± 0.09	0.49 ± 0.08
J2247.9+4413	16.99 ± 0.02	18.32 ± 0.16	3.8 ± 0.9	0.370	0.34 ± 0.07	0.41 ± 0.09
J2304.7+3705	17.16 ± 0.03	> 19.2		0.222	> 0.35	

Notes. Columns: (1) source name in 3FHL catalogue, (2) magnitude of the AGN nucleus, (3) magnitude of the host galaxy, (4) effective radius of the host galaxy, (5) galactic absorption from [Schlafly & Finkbeiner \(2011\)](#), (6) redshift derived from the host galaxy brightness and (7) redshift derived through the Kormendy relation.

† Not estimated due to morphological anomalies.

ular to the line connecting the galaxy to 3FHL J1150.5+4154. We first extracted all targets brighter than certain magnitude m_c and within a certain radius r of 3FHL J1150.5+4154 using the Source Extractor ([Bertin & Arnouts 1996](#)) and recorded their positions, ellipticities ϵ and position angles. Then we calculated ϕ , the angle between the target major axis and the line connecting the target to 3FHL J1150.5+4154, and plotted ϕ as a function of ϵ . In case of strong distortions by lensing it is expected that at low ϵ , where the targets are mostly stars, ϕ is independent on ϵ , but as ϵ gets higher the ϕ values are more concentrated around 90 degrees. We tested different values of m_c and r , but in all cases the distribution of ϕ remained uniform, even at high ellipticities. We thus found no evidence of preferred orientation of galaxies around 3FHL J1150.5+4154.

6. Discussion

In this section, we compare the redshift constraints obtained in this work with other redshift constraints. As the redshifts we determined in this work with the two methods agree in all cases

very well within the uncertainties, in the following comparisons we only report z_1 for simplicity.

In 5 cases out of 9 where we detected the host galaxy, we have also the spectroscopic redshift from [Paiano et al. \(2020\)](#) or [Kasai et al. \(2023\)](#). Table 4 lists those cases together with earlier estimates from the literature. The photometric and spectroscopic redshifts are compared in Fig. 6. This figure shows that the host galaxy method is able to provide a reasonable estimate of the blazar redshift at least up to $z=0.5$. Beyond that, the redshifts seem to be underestimated by the host galaxy method, but there are only three data points, so it is unclear how significant this offset is. Such a deviation is expected since at redshifts beyond 0.5 we are likely to detect only the most luminous host galaxies, brighter than the assumed $M_R = -22.7$.

This can in fact be seen from Table 5 where we have computed the R-band host galaxy luminosity and estimated the central black hole masses of the 5 targets with a spectroscopic redshift. To estimate the black hole masses we first transformed our K- and evolution corrected I-band absolute magnitudes to the R-band using $M_R = M_I + 0.62$. We then used two different bulge-

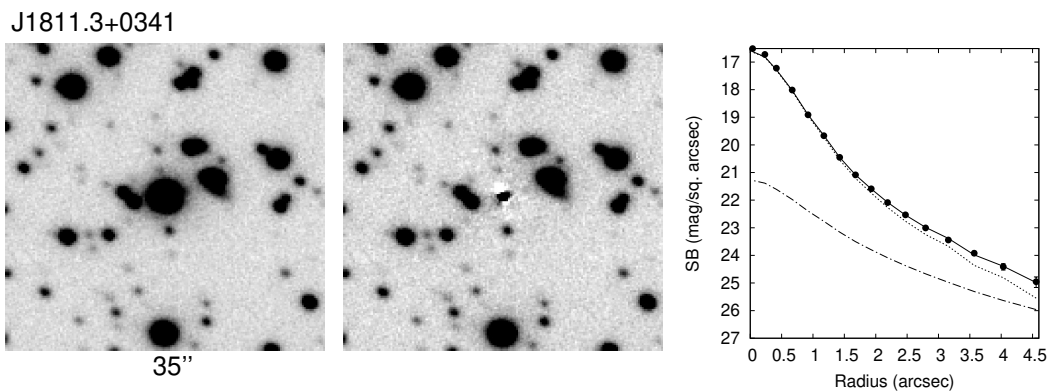


Fig. 3. Results of the AGN + host galaxy decomposition of J1811+0341. The panels are the same as in Fig. 2.

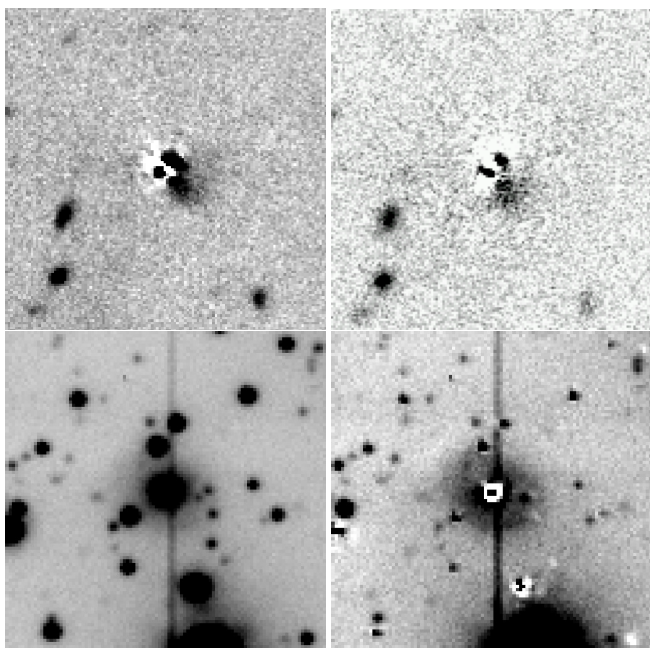


Fig. 4. *Upper row, left:* 3FHL J0915.9+2933 after subtracting the PSF + host galaxy model. The field of view is 27×27 arcsec. *Upper row, right:* the same target from Nilsson et al. (2003). *Lower row, left:* a 21×21 arcsec field around 3FHLJ 1933.3+0726. *Lower row, right:* The same field after subtracting the PSF from bright sources in the field and from the blazar.

luminosity - BH mass relationships, the $M_R - M_{BH}$ correlations of Graham (2007) and Jiang et al. (2011) to compute the black hole masses. The two estimates agreed to within 0.1 in dex. In Table 5 we give the average of the two results. As can be seen from the table, in 4 out of 5 cases the luminosity of the host galaxy is brighter than the average luminosity $M_R = -22.7$, in three cases even more than the $\sigma = 0.5$ of the host galaxy absolute magnitude distribution.

On the other hand, some targets in our 17 target sample have been imaged before with negative results. Thus, one might argue that because of this, the bright host galaxies have already been detected and we should be finding on average fainter host galaxies. Shaw et al. (2013) discussed this as one possible explanation why they derived fainter average magnitude ($M_R = -22.5$) for their host galaxies compared to earlier work by Sbarufatti et al. (2005a) ($M_R = -22.9$). In our case, none of the five targets had previous imaging observations and the sample is too small to make any statement to support one or the other average magni-

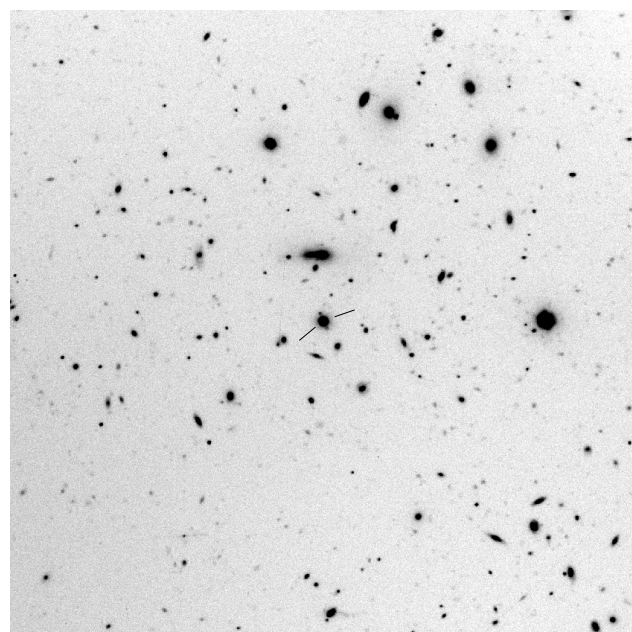


Fig. 5. 4.3×4.3 arcmin field around 3FHL J1150.5+4154. The blazar is indicated by tick marks.

tude. But it is certainly interesting that in this very small sample, the very luminous host galaxies are "over-represented". We encourage further deep imaging observations of high-synchrotron-peaked sources with known spectroscopic redshift to further investigate this issue.

In addition to direct spectroscopic constraints on redshifts and the host galaxy imaging discussed in this paper, it is also possible to obtain constraints on the blazar redshift from the spectroscopic redshifts of galaxies close to the blazar. This method has been used for several blazar previously: PKS 0447-439 ($z=0.343$, Muriel et al. 2015), PKS 1424+240 ($z=0.601$, Rovero et al. 2016), PG 1553+113 ($z=0.433$, Johnson et al. 2019) which is also in our sample (3FHL J1555.7+1111), and RGB 2243+203 ($z=0.528$, Rosa González et al. 2019). In the case of PKS 1424+240, direct spectroscopic observations have later confirmed the redshift (Paiano et al. 2017; D'Ammando et al. 2024). We did not perform dedicated spectroscopy of the companions, but eight of the blazars in our sample are within the SDSS footprint and we searched the SDSS database to obtain the redshifts of the galaxies within 7.5 arcmin of the target blazar. We selected this radius, because at $z=0.3$ this radius corresponds to approximately 2 Mpc, which is a typical search

Table 4. Comparison of host galaxy based redshift estimates to spectroscopically measured redshifts. The upper part lists earlier imaging results, whereas the lower part refers to the results presented in this paper.

(1) Target	(2) z_{phot}	(3) ref	(4) z_{spec}	(5) ref
RGBJ0115+253	0.35 ± 0.05	2	0.376	3
RGBJ0202+088	0.55 ± 0.05	2	0.629	10
RGBJ0227+020	0.45 ± 0.05	2	0.458	4
RGBJ0250+172	0.25 ± 0.05	2	0.243	3
RGBJ0505+042	0.35 ± 0.05	2	0.424	11
PKS0735+178	0.45 ± 0.06	6	0.424	7
RGBJ0757+099	0.30 ± 0.05	2	0.266	3
RGBJ1415+485	0.50 ± 0.05	2	0.496	5
3FHLJ0045.3+2127	0.34 ± 0.07	1	0.4253	8
3FHLJ0148.2+5201	0.38 ± 0.07	1	0.437	8
3FHLJ0905.5+1357	0.50 ± 0.09	1	0.644*	8
3FHLJ2031.0+1936	0.39 ± 0.08	1	0.3665	9
3FHLJ2245.9+1545	0.44 ± 0.09	1	0.5966	9

Notes. * See section 6.1 for details about the redshift values.

References: (1) This work, (2) Nilsson et al. (2003), (3) La Mura et al. (2022), (4) Sbarufatti et al. (2005b), (5) SDSS DR3, (6) Nilsson et al. (2012), (7) Mishra et al. (2018), (8) Paiano et al. (2020), ¹ (9) Kasai et al. (2023), (10) Shaw et al. (2012) (11) Pita et al. (2014)

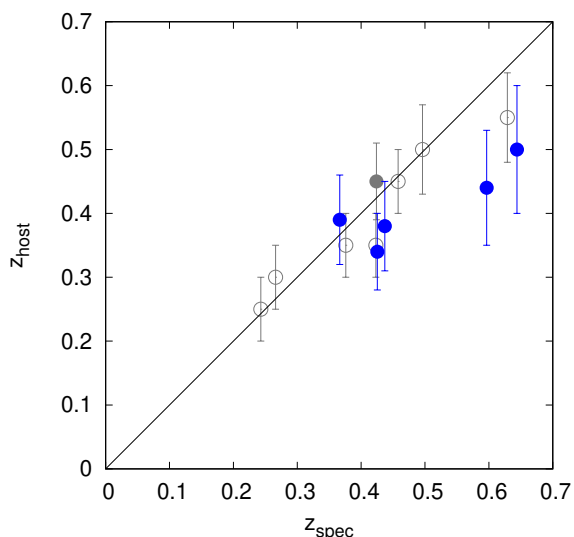


Fig. 6. Comparison of redshifts obtained spectroscopically and the host galaxy method. Grey symbols show earlier results and blue symbols the results obtained in this paper. Open symbols denote R-band detections, filled symbols I-band (see Tab. 4 and the text for details). The line shows perfect correspondence.

radius for companion galaxies (see e.g. Massaro et al. 2020a). According to mock sample simulations of Massaro et al. (2019, 2020b), if there are two companions at the same redshift (within $z < 0.05$) within 1.0 Mpc from the blazar and/or 4 companions within 2 Mpc, the probability that the blazar is associated to that group is higher than 95%. Their studies extend only to redshift of 0.15 and are therefore not directly applicable to our objects that are at higher redshifts. Nevertheless, we search for companion galaxies within these two radii. The redshifts of the companion galaxies, with their distance to the central blazar are reported in Appendix B. Figure 7 shows the two best examples of companion galaxy redshift distribution. Interestingly, we find for seven

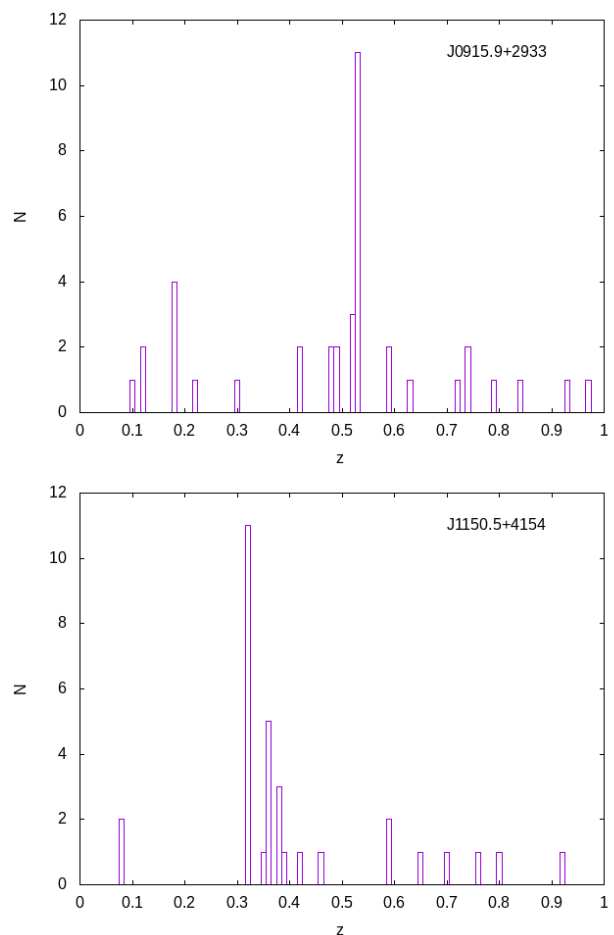


Fig. 7. Histograms of companion galaxy redshifts. The redshift bins are 0.01 and the histograms are shown only for the sources that have five or more galaxies in one of the redshift bin.

objects a group of four or more galaxies within 7.5 arcmin from the blazar. The only object for which we do not find any such group is 3FHL J1555.7+1111 which may be linked to the weakness of the galaxies composing the group found by Johnson et al. (2019). In the case of 3FHL J1546.1+0818 the group is at redshift < 0.1 and therefore likely to be a foreground group. More detailed comparison for individual objects can be found below.

We also investigated our images searching for faint galaxies that could be observed with dedicated spectroscopic observations. However, many of the objects that are not within SDSS footprint are in very crowded galactic fields (3FHL J1811.3+0341, 3FHL J1931.1+0937, 3FHL J1933.3+0726, 3FHL J1942.7+1033 and 3FHL J2031.0+1936) and identifying faint galaxies in these fields was challenging even from our deep images.

6.1. Notes on individual sources

- 3FHL J0045.3+2127: Spectroscopic redshift $z=0.4253$ (Paiano et al. 2020). As our imaging redshift is 0.34 ± 0.07 , the host galaxy of this object is more luminous than average host galaxies of BL Lac objects. In SDSS we also find 5 galaxies within 0.6 Mpc (assuming $z=0.42$) from the source, suggesting that the source is a member of rather rich group of galaxies.
- 3FHL J0148.2+5201: Spectroscopic redshift $z=0.437$ (Paiano et al. 2020). As our imaging redshift is 0.38 ± 0.07 ,

Table 5. R-band host galaxy luminosity and estimated the central black hole masses.

(1)	(2)	(3)	(4)	(5)	(6)
3FHL name	z	M_R	r_{eff} (kpc)	$\log(M_{\text{BH}}/M_{\odot})$	ref
J0045.3+2127	0.4253	-23.3 ± 0.1	9.5 ± 1.1	8.7	1
J0148.2+5201	0.437	-23.1 ± 0.1	4.5 ± 1.1	8.6	1
J0905.5+1357	0.2239	-20.7 ± 0.1	5.7 ± 1.8	8.0	}1
	0.644	-23.4 ± 0.2	11.0 ± 3.5	8.7	
J2031.0+1936	0.3665	-22.6 ± 0.1	9.1 ± 1.5	8.5	2
J2245.9+1545	0.5966	-23.6 ± 0.3	16.0 ± 3.3	8.8	2

Notes. Columns: (1) source name in 3FHL catalogue, (2) redshift, (3) absolute magnitudes, (4) effective radii, (5) black hole mass, (6) redshift reference.

References: (1) [Paiano et al. \(2020\)](#), (2) [Kasai et al. \(2023\)](#).

the host galaxy is on the brightest edge of the host galaxy brightness distribution. The source is outside of the SDSS footprint.

- 3FHL J0905.5+1357: Two spectroscopic observations separated by about one year interval led to the detection of one emission line. If this line is interpreted as [OIII]b, then $z=0.2239$, while if interpreted as [OII] then $z=0.644$ ([Paiano et al. 2020](#)). Our imaging result is 0.50 ± 0.09 . The calculated absolute magnitudes of the host galaxy assuming the two spectroscopic values show that if at $z=0.2239$, the galaxy is very faint ($M_R=-20.9$), and we therefore consider $z=0.644$ the more likely redshift, even if this indicates a very luminous host galaxy $M_R = -23.4$. We note that even if outside the range suggested by [Sbarufatti et al. \(2005a\)](#) ($M_R = -22.9$, $\sigma = 0.5$), the derived M_R at $z=0.644$ is as bright as the host galaxy of J2245.9+1545. In SDSS we find no galaxies at redshift close to 0.22 within 5 arcsec from the blazar, but there are three galaxies with redshift of $z = 0.644 \pm 0.05$, one of which is the closest companion of the target. We note that there is a group of faint galaxies well visible in our image and for which SDSS does not give a spectroscopic redshift as they are too faint. In summary, $z=0.644$ is the likely redshift of this blazar and to establish it we suggest deep low state spectroscopic observations. Also spectroscopic observations of the faint galaxies in the field could be used to establish the presence of a group and hence constrain the redshift and characterise the environment of the BL Lac.
- 3FHL J0915.9+2933: Several featureless high S/N spectra exist ([Shaw et al. 2013](#); [Ahumada et al. 2020](#); [Paiano et al. 2017](#)). Also the determination of the imaging redshift was not successful (see Section 5). However, the field has been extensively investigated by [Wittman et al. \(2006\)](#) in their selection of clusters on the basis of weak lensing shear. They found a cluster candidate, DLCS J0916.0+2931, centred 2.5' arcmin from the position of the blazar, extending about ten arc minutes in the North-South direction. Subsequent Chandra observations detected two extended X-ray emission regions 3.2 arcmin North and 5.9 arcmin South of the blazar and a possible extended region 27 arcsec from the blazar. The Northern and Southern X-ray sub-clusters are both at $z=0.53$ from Keck optical ([Wittman et al. 2006](#)) and XMM observations ([Deshpande et al. 2017](#)). The central sub-cluster could not be detected in XMM observations due to confusion with the strong blazar emission ([Deshpande et al. 2017](#)) and optical spectroscopy of its galaxies was not performed. The presence of this extended cluster in the field argues for 3FHL J0915.9+2933 to be a high redshift gamma-ray blazar. In SDSS the closest galaxy has redshift 0.489 (assuming this

redshift, it is only 200 kpc from the blazar), but within 2 arc minutes (about 800 kpc at those distances) there are also two galaxies at 0.53 like the DLCS cluster, and another one at 0.487. When we consider the whole area of 7.5 arcmin, there are in total 11 galaxies at $z \sim 0.53$. Therefore, from companion galaxy data alone, we cannot conclude the redshift. We simply note that both "candidate" redshifts from the candidate companion galaxy data are rather high. As mentioned in Section 5, the imaging observations were not done in particularly low state of the AGN and deep imaging in lower state could allow us to detect the host galaxy and estimate the redshift. However, in the case of this source, the large uncertainties of the imaging redshift would most likely contain all three possible redshift values and therefore a high S/N spectrum obtained during photometric low state would be needed to finally determine the redshift.

- 3FHL J1150.5+4154: [White et al. \(2000\)](#) claimed $z=1.01$ for this source, but in literature can be found also several featureless spectra ([Shaw et al. 2013](#); [Ahumada et al. 2020](#); [Paiano et al. 2020](#)). The last one has high signal to noise and was obtained in a relatively low state. In this work, we derive an imaging redshift of 0.46 ± 0.09 , incompatible with the high redshift suggested by [White et al. \(2000\)](#). Our result is consistent with the lower limit set by [Paiano et al. \(2020\)](#), $z > 0.25$. In SDSS, 11 nearby galaxies within 3.5 arc minutes (about 1 Mpc at $z=0.32$) have spectroscopic redshift $z \sim 0.322-0.328$. Our imaging redshift suggests that the blazar is located at higher redshift than this group or that the host galaxy of the blazar is under-luminous $M_R = -21.8$, which we also cannot exclude. However, as discussed in Section 5, there is visual indication of gravitational lensing in this field, so even if we were not able to confirm that, we note that the imaging redshift would be also consistent with the group being the gravitational lens.
- 3FHL J1546.1+0818: A spectroscopic lower limit $z \geq 0.513$ ([Ahumada et al. 2020](#)) has been obtained by SDSS. We observed it using Lick/Shane ([Kasai et al. \(2023\)](#)) but we obtained only a low S/N spectrum. The implied high redshift is in agreement with our non-detection of the host galaxy. As mentioned above already, the only group of 4 galaxies in this field has redshift of $z \sim 0.07$ and is clearly a foreground group, especially given that the spectroscopic lower limit indicates that 2 Mpc at the redshift of the blazar is smaller than 5 arcmin, while two of the galaxies of this group have a distance to the blazar greater than 6 arcmin. Within this radius there is a group of three galaxies with redshifts 0.55-0.57. The closest companion has redshift of 0.513, exactly at the redshift of the lower limit from spectroscopy and at a distance of ~ 285 kpc. In summary, we cannot conclude the red-

- shift, but our lower limit $z > 0.5$ supports the redshift estimations above.
- 3FHL J1555.7+1111: (a.k.a. PG 1553+113) is a very well known VHE γ -ray emitting blazar. There have been multiple attempts of imaging (Scarpa et al. 2000; Treves et al. 2007) and high S/N spectra (Sbarufatti et al. 2006; Aharonian et al. 2008; Landoni et al. 2014) without success. Therefore, it is not surprising that our imaging did not detect any extension of the object, especially as it was taken in a rather high state of the source (see light curves in Appendix A). For this blazar a spectroscopic lower limit $z \geq 0.4131$ was reported (Danforth et al. 2010). Furthermore it is reported to be a member of a galaxy group at $z=0.433$ (Johnson et al. 2019; Dorigo Jones et al. 2022) and this gives the strongest constraint on the redshift. Dorigo Jones et al. (2022) reported the spectroscopic redshift $z=0.408 - 0.436$ (95% confidence interval), but these galaxies are too faint for SDSS spectroscopy and therefore do not show up in our search for companions. Indeed in our deep image, we do detect many faint galaxies.
 - 3FHL J1811.3+0341: We have previously obtained two featureless medium S/N spectra (Lick/Kast, Kasai et al. 2023). As discussed in Section 5, we see some extended emission, but it is too weak to determine the redshift and resulted in $z > 0.3$. From the light curve it is evident that the timing of the imaging observations was more favourable than the timing of the spectra and therefore deeper spectroscopy should be obtained during a lower optical state to determine the spectroscopic redshift.
 - 3FHL J1844.4+1546: We derived lower limit of $z > 0.3$. We are not aware of previous constraints on the redshift of this source.
 - 3FHL J1931.1+0937: The spectroscopic lower limit $z \geq 0.476$ (Shaw et al. 2013) is in agreement with our lower limit $z > 0.2$.
 - 3FHL J1933.3+0726: As discussed in Section 5, the extension we see is unlikely to be the host galaxy of the source. Kasai et al. (2023) obtained a high S/N Keck/ESI spectrum of this target, which turned out to be featureless, i.e. showed no lines from the extension we see. 3FHL J1933.3+0726 was ~ 1 mag brighter during the epoch of the spectrum than during host imaging and the low surface brightness (~ 22.4 mag / sq. arcsec) of the nebulosity are likely to be the two main factors contributing to the non-detection in the spectrum. As the object is not within the SDSS footprint, our study does not result in new information about the redshift of the target and it remains unknown.
 - 3FHL J1942.7+1033: One featureless high S/N spectrum has been obtained with FORS/VLT (Tsarevsky et al. 2005; Masetti et al. 2013), but we clearly detect the host galaxy and obtain an imaging redshift of $z = 0.28 \pm 0.06$. As the imaging observation was done before the ZTF era, we do not know if the central AGN was in a particularly low state during the imaging, but given the rather low redshift, the spectral lines should be also detectable if spectroscopy was performed in a low state.
 - 3FHL J2031.0+1936: The spectroscopic redshift $z=0.3665$ (Kasai et al. 2023; Paiano et al. 2023) is in good agreement with our imaging result 0.39 ± 0.08 . This is in slight contradiction with the spectroscopic absolute magnitude of Kasai et al. (2023), who reported the host galaxy to be quite luminous $M_R = -23.5 \pm 0.3$, whereas our results indicate $M_R = -22.6 \pm 0.1$. We reviewed the results by the Kasai et al. (2023) and noticed that they obtain an observed magnitude $r=17.7$ for the source while ZTF obtains $r=18.1$ around this date. Correcting for this systematic difference, we would obtain $M_R = -23.1 \pm 0.3$, compatible with the imaging result. Our observations were performed during a low state of the source as was the Keck/ESI spectroscopic observation that resulted in the detection of the spectral lines and determination of the spectroscopic redshift.
 - 3FHL J2156.0+1818: A spectroscopic lower limit $z \geq 0.6347$ was obtained by D’Ammando et al. (2024). Our imaging result is in agreement, and this is the most distant host galaxy in our sample for which we have significant detection of host galaxy. We derive $z = 0.60 \pm 0.11$. There is a nearby galaxy in SDSS with $z=0.6334$ at corresponding distance of 1.16 Mpc, so very close to the spectroscopic lower limit, but at that distance it is likely not the origin of the absorber. Within the radius of 7.5 arcmin there is also one group of 4 galaxies with redshifts 0.51-0.53, but given the likely redshift of > 0.6 , all of these galaxies would be outside the 2 Mpc radii and therefore not likely to be associated to the blazar.
 - 3FHL J2245.9+1545: A spectroscopic redshift $z=0.5965$ was obtained by Kasai et al. (2023), while the imaging redshift is $z = 0.44 \pm 0.09$. So the host galaxy is very luminous, the most luminous in our sample. There is a group of four galaxies at $z = 0.43$ and the galaxy closest to the blazar belongs to that group. There are no galaxies at the redshift similar to spectroscopic redshift, but given the high redshift, they could be too faint for SDSS.
 - 3FHL J2247.9+4413: Two featureless low S/N spectra can be found in the literature (Shaw et al. 2013; Massaro et al. 2015b). A featureless medium S/N Lick/Kast spectrum was reported in Kasai et al. (2023). Our imaging observations took place before the ZTF era, so we cannot evaluate if we did catch the sources in a particularly low state, but the imaging redshift of $z = 0.34 \pm 0.07$ would indicate that with higher S/N, some lines should be detectable.
 - 3FHL J2304.7+3705: A featureless low S/N spectrum was shown in (Shaw et al. 2013) and two featureless low S/N Lick/Kast spectra in Kasai et al. (2023). We did not detect the host galaxy and the source is not within the SDSS footprint. However, we estimated the lower limit $z > 0.35$ for this target.

7. Summary and Conclusions

In this work we present the results of a deep I-band imaging program of 17 blazars, whose γ -ray flux and spectral shape make them potential targets for the CTAO. At the time of our observations, the redshifts of the sources were unknown and the primary goal was to determine imaging redshifts for them. This was done using two different methods, one using the magnitude of the host galaxy and another using both magnitude and effective radii. In addition, we obtained redshifts of galaxies near our targets from the SDSS to further constrain the blazar redshifts.

We were able to detect the host galaxy in 9 out of 17 blazars. The imaging redshifts obtained with the two methods agree within errorbars. The derived imaging redshifts range from 0.28 ± 0.06 to 0.60 ± 0.11 , with the latter (3FHL J2156.0+1818) being the most distant blazar for which the redshift has been constrained using this method. There were three targets where we detect the host galaxy, but direct spectroscopic observations have not detected any lines: 3FHL J1150.5+4154, 3FHL J1942.7+1033 and 3FHL J2247.9+4413. The derived host galaxy magnitudes and parameters indicate that all of them have

rather high nucleus to host galaxy ratio which could partially explain the non-detection of lines. Another explaining factor could be that the imaging observations were taken during lower state of the nucleus than the spectroscopic observations, but unfortunately in two of the cases the imaging observations were taken before the ZTF era and we could not evaluate this. The success of detecting the host galaxy, despite the high nucleus to host galaxy ratio, shows that in some of such cases the imaging redshift can indeed be the only viable way to get information about the source redshift.

We also showed that in the absence of a spectroscopically determined redshift it is still possible to obtain useful constraints for z by combining deep imaging, archival spectroscopic data of the galaxy environment of the blazar and spectroscopic lower limits. For instance, in the case of 3FHL J2156.0+1818 our imaging redshift 0.60 ± 0.11 was also confirmed by spectroscopic observations and we found from SDSS that there is a nearby galaxy located at similar redshift. All three constraints are in good agreement and can be combined to narrow down the redshift of the object to the range $0.63466 < z < 0.71$, with the lower limit being a "hard" limit and the upper limit being a 1 sigma limit from the host galaxy. For 3FHL J0905.5+1357, we detect a host galaxy with a magnitude that clearly favours the higher of the two possible redshifts from [Paiano et al. \(2020\)](#).

Finally, we note that in the case where we also had a spectroscopic redshift of the target and could therefore calculate the absolute magnitudes of the host galaxies, the detected hosts were brighter than what are typically detected for BL Lacs. Our sample is small and we cannot draw any conclusions from this, but this certainly serves as motivation for further studies of BL Lac host galaxies also in the future.

Acknowledgements. Based on observations made with the Nordic Optical Telescope, owned in collaboration by the University of Turku and Aarhus University, and operated jointly by Aarhus University, the University of Turku and the University of Oslo, representing Denmark, Finland and Norway, the University of Iceland and Stockholm University at the Observatorio del Roque de los Muchachos, La Palma, Spain, of the Instituto de Astrofísica de Canarias. The data presented here were obtained with ALFOSC, which is provided by the Instituto de Astrofísica de Andalucía (IAA) under a joint agreement with the University of Copenhagen and NOT. Part of this work was supported by the German *Deutsche Forschungsgemeinschaft*, DFG project number Ts 17/2-1 and Academy of Finland projects 317636, 320045, 346071, and 322535. Funding for the SDSS and SDSS-II has been provided by the Alfred P. Sloan Foundation, the Participating Institutions, the National Science Foundation, the U.S. Department of Energy, the National Aeronautics and Space Administration, the Japanese Monbukagakusho, the Max Planck Society, and the Higher Education Funding Council for England. The SDSS Web Site is <http://www.sdss.org/>. The SDSS is managed by the Astrophysical Research Consortium for the Participating Institutions. The Participating Institutions are the American Museum of Natural History, Astrophysical Institute Potsdam, University of Basel, University of Cambridge, Case Western Reserve University, University of Chicago, Drexel University, Fermilab, the Institute for Advanced Study, the Japan Participation Group, Johns Hopkins University, the Joint Institute for Nuclear Astrophysics, the Kavli Institute for Particle Astrophysics and Cosmology, the Korean Scientist Group, the Chinese Academy of Sciences (LAMOST), Los Alamos National Laboratory, the Max-Planck-Institute for Astronomy (MPIA), the Max-Planck-Institute for Astrophysics (MPA), New Mexico State University, Ohio State University, University of Pittsburgh, University of Portsmouth, Princeton University, the United States Naval Observatory, and the University of Washington. This work was conducted in the context of the CTAO Consortium.

References

Abdollahi, S., Acero, F., Ackermann, M., et al. 2020, *ApJS*, 247, 33
 Abraham, R. G., McHardy, I. M., & Crawford, C. S. 1991, *MNRAS*, 252, 482
 Aharonian, F., Akhperjanian, A. G., Barres de Almeida, U., et al. 2008, *A&A*, 477, 481
 Ahumada, R., Allende Prieto, C., Almeida, A., et al. 2020, *ApJS*, 249, 3
 Ajello, M., Angioni, R., Axelsson, M., et al. 2020, *ApJ*, 892, 105

Ajello, M., Atwood, W. B., Baldini, L., et al. 2017, *ApJS*, 232, 18
 Bertin, E. & Arnouts, S. 1996, *A&AS*, 117, 393
 Chambers, K. C., Magnier, E. A., Metcalfe, N., et al. 2016, arXiv e-prints, arXiv:1612.05560
 Cherenkov Telescope Array Consortium, Acharya, B. S., Agudo, I., et al. 2019, Science with the Cherenkov Telescope Array (World Scientific Publishing Co. Pte. Ltd.)
 D'Ammando, F., Goldoni, P., Max-Moerbeck, W., et al. 2024, arXiv e-prints, arXiv:2401.07911
 Danforth, C. W., Keeney, B. A., Stocke, J. T., Shull, J. M., & Yao, Y. 2010, *ApJ*, 720, 976
 Deshpande, A. J., Hughes, J. P., & Wittman, D. 2017, *ApJ*, 839, 124
 Domínguez, A., Primack, J. R., Rosario, D. J., et al. 2011, *MNRAS*, 410, 2556
 Dorigo Jones, J., Johnson, S. D., Muzahid, S., et al. 2022, *MNRAS*, 509, 4330
 Fioc, M. & Rocca-Volmerange, B. 2019, *A&A*, 623, A143
 Fukugita, M., Shimasaku, K., & Ichikawa, T. 1995, *PASP*, 107, 945
 Ghisellini, G., Tavecchio, F., Foschini, L., & Ghirland, A. G. 2011, *MNRAS*, 414, 2674
 Goldoni, P., Pita, S., Boisson, C., et al. 2021, *A&A*, 650, A106
 Graham, A. W. 2007, *MNRAS*, 379, 711
 IceCube Collaboration, Aartsen, M. G., Ackermann, M., et al. 2018, *Science*, 361, eaat1378
 Jiang, Y.-F., Greene, J. E., & Ho, L. C. 2011, *ApJ*, 737, L45
 Johnson, S. D., Mulchaey, J. S., Chen, H.-W., et al. 2019, *ApJ*, 884, L31
 Kasai, E., Goldoni, P., Pita, S., et al. 2023, *MNRAS*, 518, 2675
 La Mura, G., Becerra Gonzalez, J., Chiaro, G., Ciroti, S., & Otero-Santos, J. 2022, *MNRAS*, 515, 4810
 Landoni, M., Falomo, R., Treves, A., & Sbarufatti, B. 2014, *A&A*, 570, A126
 Mannucci, F., Basile, F., Poggianti, B. M., et al. 2001, *MNRAS*, 326, 745
 Masetti, N., Sbarufatti, B., Parisi, P., et al. 2013, *A&A*, 559, A58
 Massaro, E., Maselli, A., Leto, C., et al. 2015a, *Ap&SS*, 357, 75
 Massaro, F., Álvarez-Crespo, N., Capetti, A., et al. 2019, *ApJS*, 240, 20
 Massaro, F., Capetti, A., Paggi, A., et al. 2020a, *ApJ*, 900, L34
 Massaro, F., Capetti, A., Paggi, A., et al. 2020b, *ApJS*, 247, 71
 Massaro, F., Landoni, M., D'Abrusco, R., et al. 2015b, *A&A*, 575, A124
 Meisner, A. M. & Romani, R. W. 2010, *ApJ*, 712, 14
 Mishra, S., Chand, H., Krishna, G., et al. 2018, *MNRAS*, 473, 5154
 Muriel, H., Sbarufatti, B., Rovero, A. C., & Pichel, A. 2015, *A&A*, 574, A101
 Nilsson, K., Pursimo, T., Heidt, J., et al. 2003, *A&A*, 400, 95
 Nilsson, K., Pursimo, T., Villforth, C., et al. 2012, *A&A*, 547, A1
 Paiano, S., Falomo, R., Treves, A., et al. 2023, *MNRAS*, 521, 2270
 Paiano, S., Falomo, R., Treves, A., & Scarpa, R. 2020, *MNRAS*, 497, 94
 Paiano, S., Landoni, M., Falomo, R., et al. 2017, *ApJ*, 837, 144
 Pita, S., Goldoni, P., Boisson, C., et al. 2014, *A&A*, 565, A12
 Rosa González, D., Muriel, H., Mayya, Y. D., et al. 2019, *MNRAS*, 482, 5422
 Rovero, A. C., Muriel, H., Donzelli, C., & Pichel, A. 2016, *A&A*, 589, A92
 Samir, R. M., Takey, A., & Shaker, A. A. 2020, *Ap&SS*, 365, 142
 Sbarufatti, B., Treves, A., & Falomo, R. 2005a, *ApJ*, 635, 173
 Sbarufatti, B., Treves, A., Falomo, R., et al. 2005b, *AJ*, 129, 559
 Sbarufatti, B., Treves, A., Falomo, R., et al. 2006, *AJ*, 132, 1
 Scarpa, R., Urry, C. M., Falomo, R., Pesce, J. E., & Treves, A. 2000, *ApJ*, 532, 740
 Schlafly, E. F. & Finkbeiner, D. P. 2011, *ApJ*, 737, 103
 Shaw, M. S., Romani, R. W., Cotter, G., et al. 2012, *ApJ*, 748, 49
 Shaw, M. S., Romani, R. W., Cotter, G., et al. 2013, *ApJ*, 764, 135
 Stickel, M., Padovani, P., Urry, C. M., Fried, J. W., & Kuehr, H. 1991, *ApJ*, 374, 431
 Treves, A., Falomo, R., & Uslenghi, M. 2007, *A&A*, 473, L17
 Tsarevsky, G., de Freitas Pacheco, J. A., Kardashev, N., et al. 2005, *A&A*, 438, 949
 Urry, C. M. & Padovani, P. 1995, *PASP*, 107, 803
 Wakely, S. P. & Horan, D. 2008, in International Cosmic Ray Conference, Vol. 3, International Cosmic Ray Conference, 1341–1344
 White, R. L., Becker, R. H., Gregg, M. D., et al. 2000, *ApJS*, 126, 133
 Wittman, D., Dell'Antonio, I. P., Hughes, J. P., et al. 2006, *ApJ*, 643, 128
 Wurtz, R., Stocke, J. T., Ellingson, E., & Yee, H. K. C. 1997, *ApJ*, 480, 547

Appendix A: Light curves of the sources

As discussed in Section 5, we obtained light curves from the ZTF for the 12 sources that were observed with NOT in ZTF era to evaluate if the imaging observations were performed in a low state of the source. We have also noted the timing of any spectroscopy done by [Kasai et al. \(2023\)](#), [D'Ammando et al. \(2024\)](#), or any high signal-to-noise spectroscopy by other authors.

Appendix B: Companion galaxies from SDSS

The redshifts of the galaxies within 7.5 arcmin of the target blazar for all blazars of our sample that are within SDSS footprint [B.1](#), [B.2](#), [B.3](#) and [B.4](#). We selected this radius, because at $z=0.3$ this radius corresponds to approximately 2 Mpc, which is a typical search radius for companion galaxies.

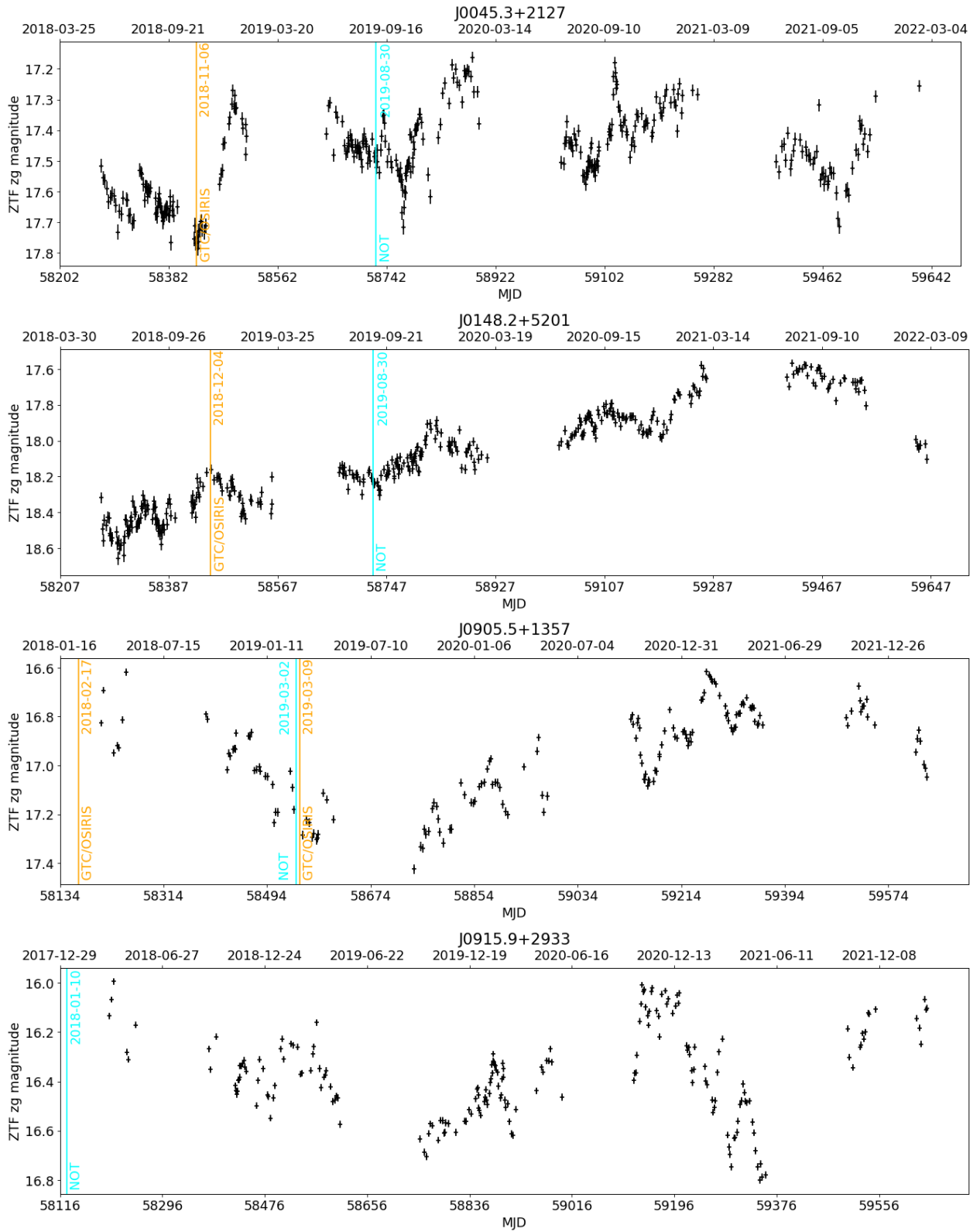


Fig. A.1. ZTF g-band light curves of J0045.3+2127 (top), J0148.2+5201, J0905.5+1357 and J0915.9+2933 (bottom). The vertical lines show the timing of spectroscopy (orange) and our deep imaging observations (magenta).

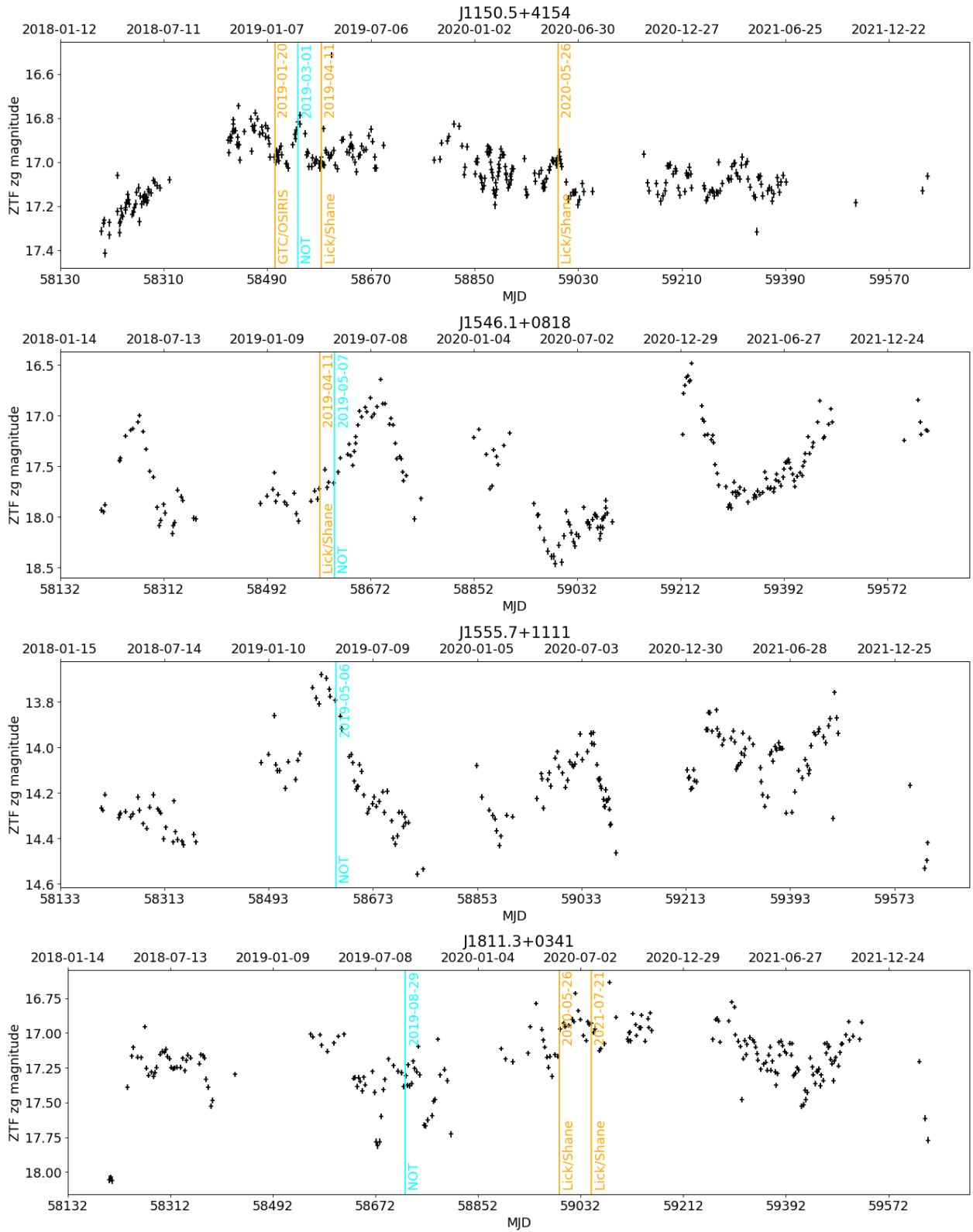


Fig. A.2. ZTF g-band light curves of J1150.5+4154(top), J1546.1+0818, J1555.7+1111 and J1811.3+0341 (bottom). The vertical lines show the timing of spectroscopy (orange) and our deep imaging observations (magenta).

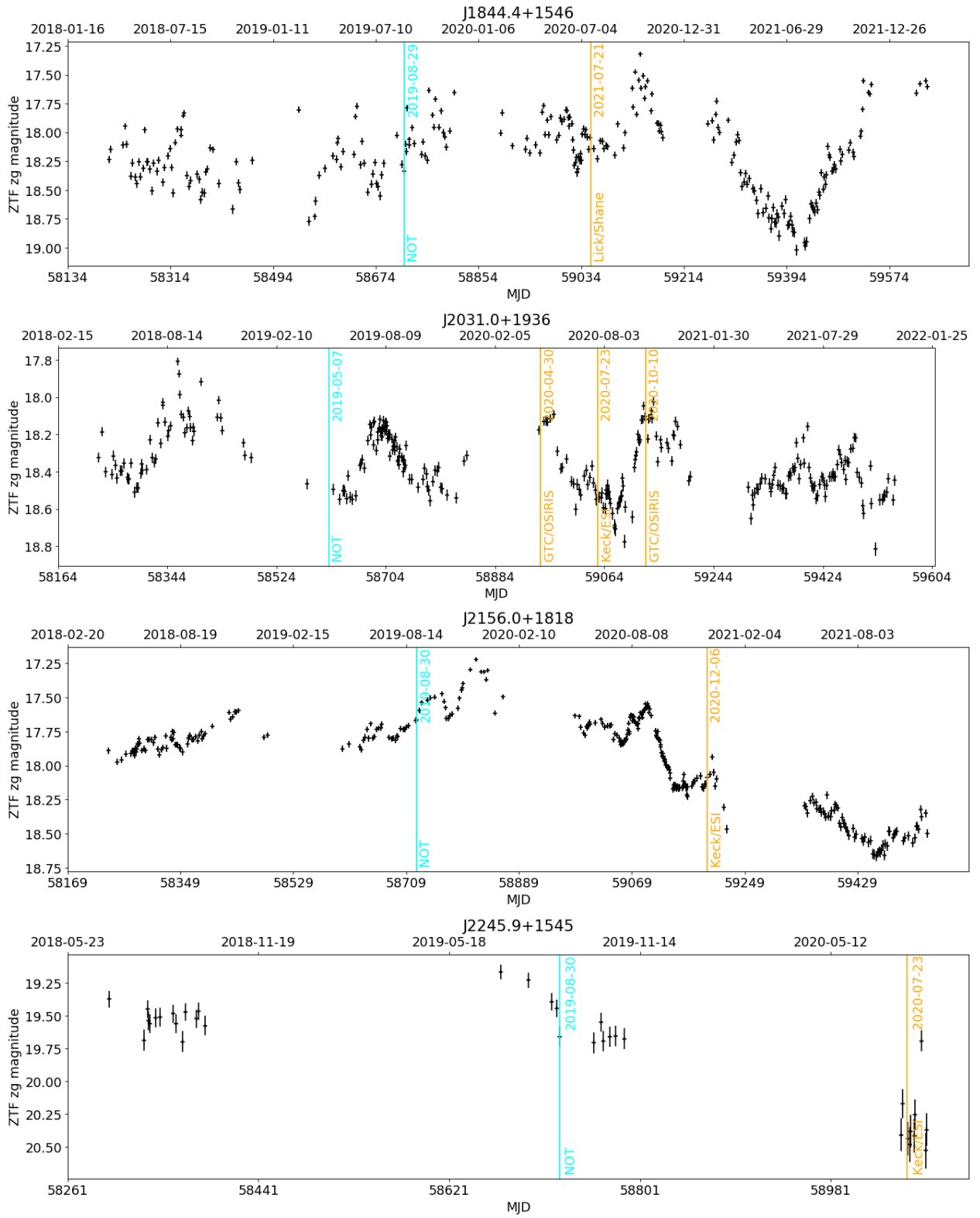


Fig. A.3. ZTF g-band light curves of J1844.4+1546(top), J2031.0+1936, J2156.0+1818 and J2245.9+1545(bottom). The vertical lines show the timing of spectroscopy (orange) and our deep imaging observations (magenta).

Table B.1. Nearby galaxies with spectroscopic redshift from SDSS

(1) 3FHL name	(2) z_{source}	(3) RA	(4) dec	(5) z_{galaxy}	(6) separation		
J0045.3+2127	0.4253	00:45:18.87	+21:27:48.08	0.426467	10.0		
		00:45:20.02	+21:26:45.52	0.421512	55.4		
		00:45:15.84	+21:26:51.28	0.425774	68.5		
		00:45:11.94	+21:28:11.57	0.620532	107.5		
		00:45:22.60	+21:26:02.00	0.321634	108.3		
		00:45:20.47	+21:29:51.39	0.418936	132.4		
		00:45:28.30	+21:28:20.41	0.062705	132.0		
		00:45:12.44	+21:26:03.95	0.430495	135.7		
		00:45:08.12	+21:28:23.96	0.400371	162.1		
		00:45:17.23	+21:24:51.63	0.321582	170.8		
		00:45:20.01	+21:31:46.68	0.709595	246.9		
		00:45:00.22	+21:24:33.11	0.482452	325.4		
		J0905.5+1357	0.2239 or 0.644	09:05:35.057	+13:58:20.107	0.6385	13.8
				09:05:30.864	+14:00:07.402	0.1641	135.1
09:05:41.167	+13:56:04.488			0.4503	151.5		
09:05:48.715	+13:58:47.626			0.3727	204.0		
09:05:19.930	+13:58:28.542			0.7636	220.3		
09:05:51.598	+13:57:11.437			0.3724	247.9		
09:05:26.714	+13:54:28.249			0.3107	249.1		
09:05:50.856	+13:59:47.058			0.3712	252.0		
09:05:46.697	+14:01:59.858			0.1784	289.1		
09:05:32.832	+13:53:06.436			0.6416	301.5		
09:05:56.551	+13:56:43.235			0.5483	324.71		
09:05:44.885	+13:53:06.850			0.3909	332.34		
09:05:12.487	+13:59:54.107			0.6935	344.78		
09:05:46.690	+14:03:22.147			0.8126	358.80		
09:05:29.191	+14:04:35.119			0.3123	397.83		
09:05:39.019	+13:51:24.998			0.3900	405.60		
09:05:52.054	+14:03:37.004			0.3255	413.56		
09:05:53.275	+13:52:42.002	0.0685	419.61				

Notes. Columns: (1) source name in 3FHL catalogue (2) spectroscopic redshift of the source (3) right ascension of the nearby galaxy (4) declination of the nearby galaxy (5) redshift of the nearby galaxy. (6) separation between the blazar and galaxy in arcsec.

Table B.2. Nearby galaxies with spectroscopic redshift from SDSS (continued)

(1) 3FHL name	(2) z_{source}	(3) RA	(4) dec	(5) z_{galaxy}	(6) separation
J0915.9+2933		09:15:52.553	+29:32:51.058	0.4886	33.0
		09:15:56.818	+29:33:9.691	0.5280	59.4
		09:15:56.990	+29:33:47.380	0.4871	64.3
		09:15:53.614	+29:32:9.856	0.5308	75.9
		09:15:46.020	+29:32:0.647	0.5942	117.9
		09:15:51.226	+29:31:8.731	0.1809	136.2
		09:16:02.798	+29:33:11.736	0.5302	136.2
		09:15:50.453	+29:35:39.426	0.1857	137.7
		09:15:55.171	+29:31:9.232	0.4243	139.6
		09:16:03.487	+29:33:12.445	0.5321	145.1
		09:15:59.945	+29:35:30.221	0.7452	160.0
		09:15:52.850	+29:36:18.529	0.5308	174.6
		09:15:52.303	+29:36:38.419	0.5322	194.4
		09:15:47.851	+29:36:49.381	0.5316	213.7
		09:15:34.733	+29:32:29.987	0.9701	236.8
		09:16:03.228	+29:29:51.907	0.5323	254.9
		09:15:59.791	+29:37:32.707	0.5310	266.7
		09:15:52.642	+29:28:54.048	0.7465	270.0
		09:16:08.446	+29:36:40.428	0.1226	287.0
		09:15:33.624	+29:36:6.710	0.2207	294.0
		09:16:06.506	+29:37:15.168	0.8410	295.4
		09:16:15.456	+29:32:23.852	0.5984	306.8
		09:15:57.502	+29:28:22.415	0.5266	308.9
		09:15:32.918	+29:36:28.645	0.7966	314.1
		09:15:42.578	+29:38:32.377	0.5332	333.9
		09:15:52.212	+29:39:1.134	0.1027	337.1
		09:16:00.634	+29:28:4.505	0.5255	337.1
		09:15:43.574	+29:27:55.858	0.9368	347.8
		09:16:01.063	+29:27:50.094	0.5306	352.6
		09:15:44.945	+29:39:23.922	0.1855	372.8
		09:15:28.356	+29:37:1.740	0.7279	381.8
		09:15:23.623	+29:35:0.960	0.3016	387.8
		09:16:07.735	+29:27:42.023	0.5327	396.3
		09:15:54.151	+29:26:45.715	0.4924	399.0
		09:16:06.017	+29:27:13.291	0.4983	411.2
		09:16:24.396	+29:33:28.015	0.4239	417.5
		09:15:33.175	+29:27:43.859	0.1862	422.7
		09:15:57.782	+29:26:26.459	0.1220	423.5
		09:15:44.366	+29:40:41.045	0.6324	449.4

Notes. Columns: (1) source name in 3FHL catalogue (2) spectroscopic redshift of the source (3) right ascension of the nearby galaxy (4) declination of the nearby galaxy (5) redshift of the nearby galaxy. (6) separation between the blazar and galaxy in arcsec.

Table B.3. Nearby galaxies with spectroscopic redshift from SDSS (continued)

(1) 3FHL name	(2) z_{source}	(3) RA	(4) dec	(5) z_{galaxy}	(6) separation
J1150.5+4154	0.42 ± 0.09	11:50:36.214	+41:54:32.450	0.3219	18.0
		11:50:34.855	+41:55:07.255	0.3268	27.1
		11:50:32.170	+41:55:34.568	0.3272	61.6
		11:50:27.955	+41:55:22.228	0.5970	86.8
		11:50:32.371	+41:56:05.525	0.3250	89.4
		11:50:42.305	+41:55:33.946	0.3217	100.0
		11:50:22.380	+41:54:50.735	0.3608	138.5
		11:50:25.661	+41:52:57.367	0.3271	144.5
		11:50:34.848	+41:51:58.496	0.3807	161.6
		11:50:25.867	+41:56:49.470	0.3252	163.0
		11:50:20.578	+41:53:58.740	0.3652	163.6
		11:50:31.829	+41:57:24.732	0.3253	167.8
		11:50:48.744	+41:53:04.834	0.3266	183.0
		11:50:18.442	+41:54:01.580	0.3621	186.1
		11:50:47.858	+41:56:58.250	0.3267	201.2
		11:50:30.473	+41:58:00.800	0.3288	206.3
		11:50:53.210	+41:55:35.159	0.7656	213.2
		11:50:15.578	+41:54:26.496	0.3818	214.5
		11:50:17.412	+41:56:19.828	0.3625	217.7
		11:50:44.470	+41:58:08.357	0.3557	234.8
		11:50:45.125	+41:58:04.649	0.6549	235.0
		11:50:13.882	+41:53:01.162	0.0881	253.2
		11:50:46.934	+41:50:54.812	0.8034	263.2
		11:50:11.328	+41:54:02.070	0.5988	264.3
		11:50:15.847	+41:50:42.788	0.9279	317.7
		11:50:34.716	+41:49:20.528	0.4279	319.6
		11:50:07.111	+41:53:07.721	0.3900	322.2
		11:50:16.092	+41:59:13.859	0.3821	343.9
		11:51:04.462	+41:52:58.508	0.7068	346.9
		11:50:03.782	+41:53:58.661	0.4636	348.2
		11:50:07.536	+41:58:10.909	0.3627	369.7
		11:49:58.819	+41:57:26.309	0.0822	434.0
		<hr/>			
J1546.1+0818		15:46:04.963	+08:18:28.426	0.5130	46.2
		15:46:09.413	+08:19:11.418	0.0703	76.6
		15:45:54.648	+08:18:29.725	0.5516	149.1
		15:45:54.101	+08:18:38.553	0.5617	154.6
		15:46:12.605	+08:22:41.919	0.0407	242.6
		15:46:17.738	+08:16:23.605	0.0701	262.5
		15:45:56.302	+08:14:59.339	0.0418	280.1
		15:46:03.281	+08:14:26.052	0.1241	287.7
		15:46:19.301	+08:22:20.667	0.4866	291.5
		15:46:23.918	+08:19:54.791	0.5076	294.8
		15:46:07.922	+08:14:22.628	0.5717	295.8
		15:46:07.572	+08:24:06.090	0.3548	296.8
		15:45:44.873	+08:17:21.636	0.2020	308.6
		15:45:43.118	+08:15:53.668	0.0707	371.9
		15:45:46.430	+08:23:37.036	0.6908	373.4
		15:46:27.041	+08:15:29.236	0.0677	405.8

Notes. Columns: (1) source name in 3FHL catalogue (2) imaging redshift of the source (3) right ascension of the nearby galaxy (4) declination of the nearby galaxy (5) redshift of the nearby galaxy. (6) separation between the blazar and galaxy in arcsec.

Table B.4. Nearby galaxies with spectroscopic redshift from SDSS (continued)

(1) 3FHL name	(2) z_{source}	(3) RA	(4) dec	(5) z_{galaxy}	(6) separation		
J1555.7+1111		15:55:43.951	+11:11:56.796	0.4343	35.1		
		15:55:33.238	+11:10:11.176	0.5054	161.8		
		15:55:58.022	+11:11:44.030	0.0415	221.3		
		15:55:42.890	+11:7:40.019	0.1520	224.4		
		15:55:26.585	+11:11:54.992	0.1056	244.1		
		15:55:53.095	+11:7:23.851	0.4320	282.4		
		15:55:59.237	+11:8:48.437	0.1513	284.8		
		15:56:0.581	+11:13:57.014	0.1354	299.8		
		15:55:21.055	+11:8:39.419	0.0450	363.2		
		15:56:1.368	+11:15:52.780	0.1344	380.4		
		15:55:18.355	+11:14:49.841	0.1516	417.3		
		15:55:19.390	+11:7:26.260	0.0707	421.8		
	J2156.0+1818	$0.60 \pm 0.10(i)$	21:56:08.570	+18:19:53.508	1.0803	124.8	
			21:56:12.041	+18:17:13.772	0.6334	170.0	
21:56:15.358			+18:20:25.573	0.1837	223.4		
21:55:53.494			+18:22:42.362	0.3181	271.3		
21:55:44.544			+18:16:9.005	0.4826	285.0		
21:55:59.993			+18:13:44.101	0.3082	294.0		
21:56:23.405			+18:16:12.281	0.6711	342.1		
21:55:53.318			+18:24:13.424	0.5136	356.5		
21:56:28.831			+18:19:18.649	0.5336	389.4		
21:55:51.967			+18:11:42.140	0.5123	437.3		
21:56:17.321			+18:24:57.895	0.5107	441.4		
J2245.9+1545			0.5965(s)	22:45:55.356	+15:45:28.487	0.4347	148.8
				22:46:07.939	+15:41:52.217	0.3241	168.6
				22:46:00.634	+15:48:04.010	0.4939	217.9
	22:45:58.769	+15:48:29.354		0.6065	250.6		
	22:45:46.406	+15:43:46.387		0.4334	272.7		
	22:45:44.330	+15:45:32.278		0.2035	303.6		
	22:45:48.482	+15:47:44.052		0.6414	303.9		
	22:45:45.475	+15:46:35.065		0.5197	306.1		
	22:45:45.780	+15:48:09.752		0.3238	350.5		
	22:45:55.370	+15:50:12.350		0.4318	364.4		
	22:45:37.039	+15:45:25.632		0.2334	406.6		
	22:46:31.896	+15:46:43.226		0.4326	408.9		
	22:45:45.797	+15:49:51.625		0.6259	420.4		
	22:46:33.732	+15:46:44.278		0.4581	434.5		

Notes. Columns: (1) source name in 3FHL catalogue (2) redshift of the source, (s)=spectroscopic, (i)=imaging (3) right ascension of the nearby galaxy (4) declination of the nearby galaxy (5) redshift of the nearby galaxy. (6) separation between the blazar and galaxy in arcsec.